GEOPHYSICS, VOL. 89, NO. 1 (JANUARY-FEBRUARY 2024); P. WB35–WB56, 23 FIGS., 4 TABLES.
10.1190/GEO2023-0213.1

Check for updates

Downloaded 12/28/23 to 77.169.250.78. Redistribution subject to SEG license or copyright; see Terms of Use at http://library.seg.org/page/policies/terms
DOI:10.1190/geo2023-0213.1

Integrating earthquake-based passive seismic methods in mineral exploration: Case study from the Gerolekas bauxite mining area, Greece

Katerina Polychronopoulou[1], Michal Malinowski[2], Marta Cyz[3], Nikos Martakis[4], George Apostolopoulos[5], and Deyan Draganov[6]

ABSTRACT

As the global need for aluminum constantly rises, bauxite is considered to be a critical mineral, and the mining industry is in search of new and effective exploration solutions. In this context, we design and implement a purely earthquake-based passive seismic survey at the Gerolekas bauxite mining site in Greece. It is a very difficult exploration setting, characterized by rough topography, limited accessibility, and a very complex geotectonic regime. We gather a passive seismic data set consisting of four months of continuous recordings (May to August 2018) from 129 stand-alone 3C seismological stations. We then analyze this data set and extract 848 microearthquakes that will serve as sources for the application of local earthquake tomography (LET) and transient-source seismic interferometry (TSI) by autocorrelation. We apply LET to estimate the 3D P- and S-wave velocity models of the subsurface below the study area and TSI by autocorrelation to retrieve the zero-offset virtual reflection responses below each of the recording stations. The velocity models provide a relatively coarse image of a previously completely unexplored part of the mining concession, whereas the higher-resolution virtual reflection imaging illuminates in detail the different interfaces. We also reprocess three lines of legacy active seismic data that were shot in 2003, using the LET P-wave velocity model for depth migration, and confirm the improvement of seismic imaging. Finally, we evaluate the obtained results using well data and jointly interpret them, extracting useful information on the expected target depths and indicating that earthquake-based passive seismic techniques can be an innovative and environmentally friendly option for mineral exploration.

INTRODUCTION

Critical minerals are a key component of the technological advances, energy orientation, and economic growth of human societies. However, as the need for critical minerals constantly rises and the known deposits are steadily depleted, the quest for fresh deposits becomes more and more demanding and challenging. Critical mineral targets become deeper, often located in complex geologic settings or environmentally sensitive areas, and their importance makes it necessary for mineral exploration to adapt and provide efficient solutions for their discovery and exploitation.

Such a case is the Gerolekas bauxite mining site in Central Greece. It is one of the major bauxite-producing areas of Europe, and despite the fact that the broader area has been extensively explored and exploited for decades — uncovering tones of bauxite — there is a part of the mining concession where there is absolutely no information on the subsurface. This part, which is affected by a significant stratigraphic overlap that altered the normal stratigraphic

Manuscript received by the Editor 30 March 2023; revised manuscript received 28 September 2023; published ahead of production 9 October 2023; published online 13 December 2023.
[1]National Technical University of Athens, School of Mining and Metallurgical Engineering, Department of Mining Engineering, Athens, Greece and Seismotech S.A., Athens, Greece. E-mail: kpolychro@seismotech.gr (corresponding author).
[2]Polish Academy of Sciences, Institute of Geophysics, Warsaw, Poland and Geological Survey of Finland, Espoo, Finland. E-mail: michal.malinowski@gtk.fi.
[3]Geological Survey of Finland, Espoo, Finland. E-mail: marta.cyz@gtk.fi.
[4]Seismotech S.A., Athens, Greece. E-mail: nmartakis@seismotech.gr.
[5]National Technical University of Athens, School of Mining and Metallurgical Engineering, Department of Mining Engineering, Athens, Greece. E-mail: gapo@metal.ntua.gr.
[6]Delft University of Technology, Department of Geoscience and Engineering, Delft, The Netherlands. E-mail: d.s.draganov@tudelft.nl.
© 2023 The Authors. Published by the Society of Exploration Geophysicists. All article content, except where otherwise noted (including republished material), is licensed under a Creative Commons Attribution 4.0 International License (CC BY). See https://creativecommons.org/licenses/by/4.0/. Distribution or reproduction of this work in whole or in part commercially or noncommercially requires full attribution of the original publication, including its digital object identifier (DOI).

Downloaded 12/28/23 to 77.169.250.78. Redistribution subject to SEG license or copyright; see Terms of Use at http://library.seg.org/page/policies/terms
DOI:10.1190/geo2023-0213.1

series, is completely unexplored, mainly due to its rough topographic relief and limited accessibility. However, taking into account the fact that the surrounding area is very rich in bauxite, geologists expect a similar situation below the Gerolekas overlap and the main question is the depth at which the allochthonous overburden is replaced with the normal series, where the bauxitic deposits are expected to lie. This depth, which according to the existing geologic scenarios is expected to be located at or below the mean sea level (MSL), is the crucial indicator that will permit the mining company to assess the exploitability of possible deposits below the unexplored area.

This question was only recently raised by the mining company exploiting the bauxite deposits in the area, because, on the one hand, this relatively low-risk greenfield exploration would offer many years of life to an important mining site nearing depletion, and, on the other hand, this is a very challenging exploration setting. The deep exploration target, which is actually not the bauxite, but a flysch-limestone interface confirming the passage to the normal series, as well as the complex geologic setting below an area characterized by significant topographic differences and limited access, led us to the design and implementation of a purely passive seismic survey in the hope of overcoming these difficulties and illuminating the Gerolekas subsurface.

Passive seismic is a broad term describing the exploitation of seismic signals that are present in a survey area for the imaging of the subsurface. These signals may be either naturally produced or anthropogenic, but they are not deliberately generated for a specific survey. The term incorporates several different methodologies, which are primarily categorized based on the type of passive seismic signal that is used and also on the scale of the survey.

The exploited signal may be naturally occurring earthquakes (Daneshvar et al., 1995; Nakata et al., 2014; Nishitsuji et al., 2016b; Orfanos et al., 2016; Polychronopoulou et al., 2019a), ambient noise (Draganov et al., 2009; Panea et al., 2014; Romero and Schimmel, 2018; Giannopoulos et al., 2019), or higher-frequency microtremors (Morton et al., 2021; Capizzi and Martorana, 2022) recorded in an area of interest. These signals are extracted from the continuous passive seismic data sets and processed to provide images of the subsurface below the study area. Numerous case studies of passive seismic surveys for exploration purposes have been shown during the past few years at a broad range of scales: from large-scale crustal studies (Nishitsuji et al., 2016a; Casas et al., 2020) to oil and gas exploration projects (Polychronopoulou and Martakis, 2016) and from smaller-scale mining exploration studies (Cheraghi et al., 2015; Polychronopoulou et al., 2019b; Chamarczuk et al., 2021) to near-surface engineering or archaeological applications (Abu Zeid et al., 2017; Morgan et al., 2022).

In the context of our research, we focused on the application of earthquake-based passive seismic methodologies that exploit naturally occurring earthquakes as seismic sources. Our aim was to provide a subsurface image of the Gerolekas area by applying a combination of different passive seismic techniques. The main challenge that we faced was the fact that our target, considered as relatively deep in terms of mining, is quite shallow in terms of earthquake seismology. Therefore, the Gerolekas survey offered a unique opportunity to explore the upper limits of the imaging ability of earthquake-based passive seismic techniques (namely, local earthquake tomography [LET] and transient-source seismic interferometry [TSI] by autocorrelation), which have never been applied at this scale. The Gerolekas seismic network consisted of 129 stand-alone stations, equipped with 3C short-period sensors, which continuously recorded during a period of four months (Figure 1). The LET and TSI rely on the detection and location of the local microearthquake sources, which we define as the naturally occurring events located within or at a very close distance from our seismic network (inside a perimeter defined by peripheral stations surrounding the study area and down to the Moho) that are characterized by very small magnitudes (even negative magnitude on the Richter scale). These events exhibit relatively higher-frequency content than typical larger-magnitude earthquakes and seismic wave emission patterns that are closer to the point-source approximation (because they are not produced by extended ruptures).

We initially apply LET — a traveltime tomography method that exploits earthquakes as sources and the passive seismic stations as receivers. In that sense, the first-arrival times of the P and S waves of local microearthquakes are used as input for tomographic inversion, which results in the estimation of 3D P- and S-wave velocity models for a subsurface volume that is spatially delineated by the horizontal dimensions of the recording seismic network and extends from the surface down to the maximum depth of occurrence of the recorded seismicity (usually at depths of several kilometers). Subsequently, we exploit the P- and S-wave coda of those of the detected microearthquakes that are located (nearly) vertically below each station. Using autocorrelation-based TSI, following the workflow described in Polychronopoulou et al. (2020), we retrieve the zero-offset virtual reflection responses, for the P and S waves, below a station under consideration, from a virtual source colocated with the station and emitting energy (nearly) vertically down. This provides a 1D passive seismic reflection image below each of the recording stations, resulting in a pseudo-3D reflection image of the study area, the spatial resolution of which, given the existence of adequate passive seismic signals, is mainly defined by the number of stations and the interstation distances of the seismic network.

Moreover, we explore the idea of evaluating the application of the 3D P-wave velocity (V_P) model derived by LET to the depth migration of legacy active seismic data. Reprocessing of existing data (mainly legacy active-source seismic data) is a practice that is nowadays becoming more and more common in mineral exploration (Malehmir et al., 2019; Manzi et al., 2019; Donoso et al., 2020). The technological advances of all exploration disciplines during the past few years often permit reprocessing of existing data using more sophisticated techniques and extracting additional information about the subsurface in a cost-effective manner.

Next, we initially present a brief overview of the Gerolekas survey and its exploration target, followed by the description of the analysis of the acquired continuous passive seismic data set and the detection and location of the microearthquake sources. We then describe the application of the two earthquake-based exploration techniques (LET and TSI by autocorrelation) to the Gerolekas data set. Subsequently, we analyze the exploitation of the obtained subsurface models for the reprocessing of legacy active-source seismic reflection data. Thus, we show an alternative contribution of a purely passive survey to the subsurface imaging of an area of interest. Following this, we attempt an integrated interpretation of these results. We jointly evaluate the different available pieces of information to provide answers to the exploration question that

Downloaded 12/28/23 to 77.169.250.78. Redistribution subject to SEG license or copyright; see Terms of Use at http://library.seg.org/page/policies/terms
DOI:10.1190/geo2023-0213.1

was set. Finally, we discuss the overall contribution of earthquake-based passive seismic techniques in mineral exploration.

THE GEROLEKAS BAUXITE MINE

The Gerolekas bauxite mining site is located in a mountainous area between the Giona and the Parnassus mountains in Central Greece (Figure 1). It is part of one of the major bauxite-producing sites of Europe. Even though the surrounding area has been extensively explored and exploited for decades, the Gerolekas site remained completely unexplored. Its topographic relief, which ranges between 300 m and 1200 m above MSL along an area of approximately 35 km^2, as well as the very limited number of mining roads that constitute the sole means of access, prevented any exploration attempts for this part of the mining concession for years.

Geologically, Gerolekas belongs to the geotectonic zone of Parnassus-Giona and is characterized by a relatively simple stratigraphy but a very complex tectonic regime. As explained in detail in Polychronopoulou et al. (2020), the normal series of the Parnassus-Giona zone consists of a superficial Paleogene flysch layer, followed by a succession of limestones of different geologic periods, dating from the Cretaceous down to the Upper Triassic, which lie above a dolomitic layer of the Middle Triassic. The bauxite deposits in the area appear in three distinct parts of the stratigraphic column and have the form of layers or lenses hosted within the carbonate rocks of the Jurassic (first and second bauxitic horizons) and the Cretaceous periods (third bauxitic horizon). From these three bauxitic horizons, the most important in terms of mining is the third bauxitic horizon, which is located closest to the surface and hosted between the limestones of the Middle and Upper Cretaceous. These limestones lie directly below the flysch-limestone interface of the Parnassus-Giona series.

Moreover, part of the Gerolekas area has been affected by a stratigraphic overlap, consisting of a limestone layer followed by Boeotian flysch, which has been tectonically set on top of the normal series. The superficial appearance of this overlap (Gerolekas nappe — limestone of the Pelagonic zone) is shown in Figure 1, defining, at the same time, the unexplored part of the survey area. Three different hypotheses exist concerning the thickness of the allochthonous layers below the Gerolekas overlap area (Figure 2). These hypotheses are presented along the profile AA′ (see profile location in Figure 1) and were constructed using information from superficial geology and the numerous wells that exist in the surrounding area. According to them, the targeted flysch-limestone interface: (1) might be located at significant depth (more than 900 m below MSL) due to the graben structure (Figure 2b), in which case, even if bauxite exists, it is of no interest for the mining company; (2) might be located at a depth close to MSL and followed by bauxite deposits similar to those of the surrounding area (Figure 2c), in which case exploitation of the bauxite deposits is possible; and (3) might be located at a depth close to MSL, but the graben structure has resulted in the entrapment of larger quantities of bauxite (Figure 2d), in which case large bauxite deposits are expected to be discovered.

THE GEROLEKAS PASSIVE SEISMIC SURVEY

Taking into account the complicated exploration conditions at the Gerolekas site, we decided to implement a purely passive survey that was the most efficient and cost-effective solution for the first exploration attempt of the subsurface below this difficult terrain. Our target was not to directly detect the bauxite deposits because it is currently impossible to image a thin layer of 1–3 m that lies at a depth of several hundreds of meters, or even deeper than 1 km, from

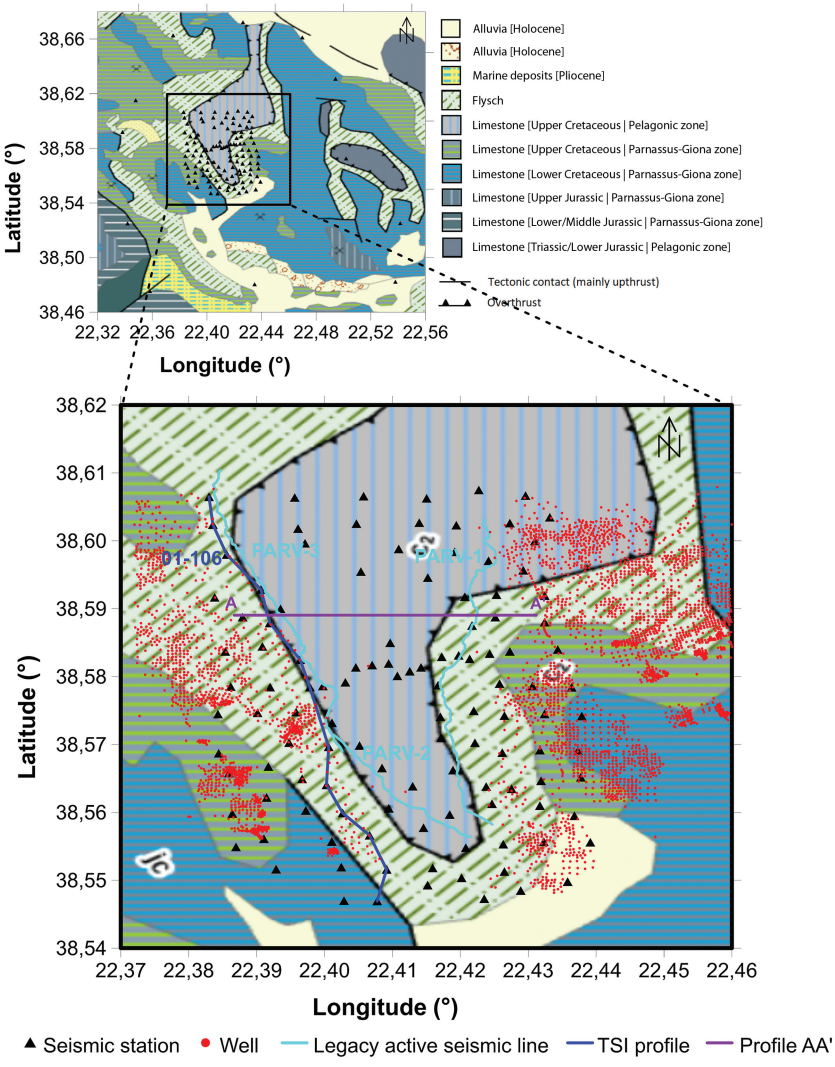

Figure 1. The Gerolekas seismic network superimposed on a geologic map of the study area (geologic map: Institute of Geology and Mineral Exploration of Greece). Black triangles correspond to the 129 stand-alone seismological stations of the network. Blue line represents the location of the TSI profile 01-106; cyan lines represent the the active-source seismic profiles PARV-1, PARV-2, and PARV-3; and red dots represent the well positions showing the explored area.

Downloaded 12/28/23 to 77.169.250.78. Redistribution subject to SEG license or copyright; see Terms of Use at http://library.seg.org/page/policies/terms
DOI:10.1190/geo2023-0213.1

the surface. Instead, our target was to delineate the flysch-limestone interface, which is indirectly linked to the appearance of the bauxitic horizon of interest and the location of which, especially below the disturbed overlap area, is completely unknown.

We installed a seismic network consisting of 129 stand-alone seismological stations (Figure 1), equipped with the same 3C short-period sensors, which are recording at a bandwidth of 0.2 (−6 dB) Hz to 98 (−3 dB) Hz. Most of the seismological stations (117 stations) were installed above the Gerolekas area (inner network), at a regular grid of approximately 500 m × 500 m, except for the parts of the study area that were completely inaccessible (see Figure 1), whereas a dozen stations were installed at distant locations surrounding the inner network. The peripheral stations served as control points, ensuring a satisfactory azimuthal coverage for the location of events occurring at the edges of the study area and a more robust estimation of hypocentral depths. The network recorded continuously during a period of four months (May to August 2018).

LOCATION OF THE PASSIVE SEISMIC SOURCES

We analyze the acquired continuous records to detect and locate the microearthquakes that occurred during the recording period within or at a distance of less than 5 km from the Gerolekas network. These microearthquakes will be our passive seismic sources for the application of LET and TSI by autocorrelation. An example of the application of the data analysis procedure on an event of the Gerolekas data set is shown in Figure 3.

First, we remove the DC component of the signals and band-pass filter the continuous records between 1 Hz and 45 Hz. The selection of the filter is based on the knowledge that the local microearthquakes are characterized by a frequency content that is significantly higher than 1 Hz and usually lower than 45 Hz (see spectrogram of Figure 3d); the 100 samples per second rate of the recording, and the consequent Nyquist frequency of 50 Hz, imposes a hard upper limit. Then, we perform event detection, using an energy-based algorithm with an improved short-time-average/long-time-average (STA/LTA) detector that uses information from all three components of each record (Leontarakis et al., 2015). The signals recorded by the three components at each station (Figure 3a) are used to estimate a characteristic function, which is then subjected to energy criteria by means of two moving windows, whereas the thresholding needed for the declaration of a candidate seismic event is dynamic and based on the statistical characteristics of the STA/LTA ratio sequence for each characteristic function. In that sense, the procedure takes into account the specific conditions prevailing at each recording site and time, which might change during the month-long recording period. The event-detection algorithm is complemented by multistation analysis, which imposes the detection of a candidate event in a predefined number of neighboring stations, taking into account the network's geometry as well as the magnitude of the events that we aim to detect (Figure 3b). Subsequently, we automatically estimate the P- and S-waves' onset time for the detected events (Figure 3c), using an algorithm that exploits the statistical characteristics of the detected signals and, more specifically, their fourth-order zero-lag cumulant kurtosis. The P-wave

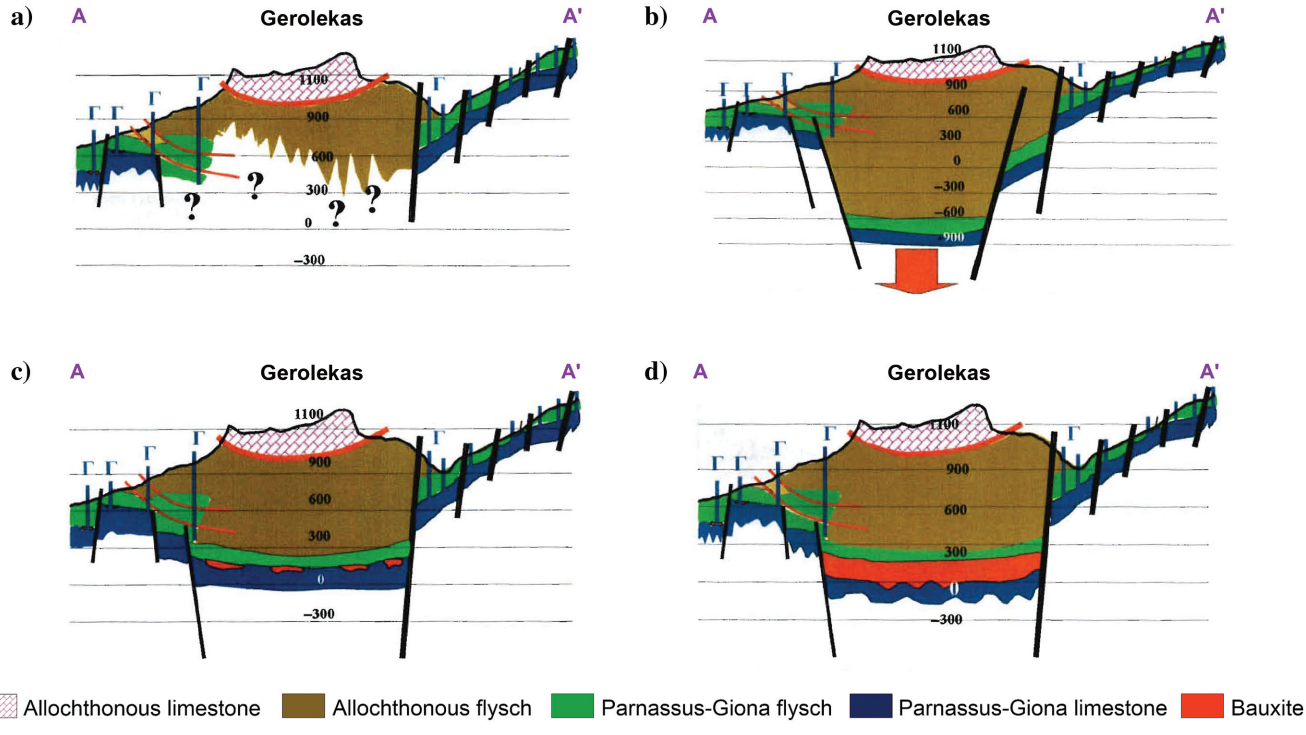

Figure 2. Geologic hypotheses regarding the thickness of the allochthonous layers below the Gerolekas overlap presented along the profile AA′ of Figure 1. (a) Known geologic features along the profile AA′. The exploration target area is marked with the question marks. (b) Hypothesis 1: the flysch-limestone interface is located at significant depth due to the graben structure. (c) Hypothesis 2: the flysch-limestone interface is located at a depth close to MSL and the bauxite deposits are similar to those of the surrounding area. (d) Hypothesis 3: the flysch-limestone interface is located at a depth close to MSL, and larger quantities of bauxite have been trapped due to the graben structure.

Downloaded 12/28/23 to 77.169.250.78. Redistribution subject to SEG license or copyright; see Terms of Use at http://library.seg.org/page/policies/terms
DOI:10.1190/geo2023-0213.1

onset time is assigned to the point where the kurtosis of the detected signal presents its maximum slope (Saragiotis et al., 2002), whereas the S-wave onset time is estimated by the application of the kurtosis criterion on the maximum eigenvalue sequence resulting from eigenvalue analysis of the 3C signal (Lois et al., 2013). We then use the obtained P- and S-wave first-arrival times to estimate the hypocentral locations of the detected earthquakes through an iterative linearized least-squares procedure.

In the case of the Gerolekas passive seismic survey, we locate 954 microearthquakes at epicentral distances of less than 5 km from at least one of the stations of the network. The duration magnitude (Md) of these earthquakes ranges between −1.5 and 2.0 on the Richter scale. Md is commonly used for estimating the magnitude of very small events, and its calculation takes into account the duration of the signals recorded during an earthquake (coda duration defined at the time between the red and green lines in Figure 3c) in relation to their epicentral distance. We further select those of the located earthquakes that are characterized by the lowest uncertainty in their location. More specifically, the selected microearthquakes satisfy the following quality criteria. (1) The estimation of their location is based on more than 10 P- and S-wave arrival times, (2) the root-mean-square (rms) error of their location solution is less than 0.15, and (3) the horizontal and vertical uncertainty of their hypocentral locations is less than 1 km. This results in a data set of 848 microearthquakes (Figure 4) that are used as the passive seismic sources for the application of LET and TSI by autocorrelation. In Figure 5, we present the statistical characteristics of the selected seismicity, in terms of hypocentral depths, number of P- and S-wave first arrivals used for locating, as well as rms errors of the earthquakes' locations.

LOCAL EARTHQUAKE TOMOGRAPHY

The 848 carefully selected microearthquakes are used as the passive seismic sources for the application of LET. We exploit the measured traveltimes of the first arrivals for the P and S waves of the located microearthquakes and invert them to estimate the P- and S-wave velocity distribution below the study area. Note that we estimate the S-wave velocity distribution indirectly by inversion for the V_P/V_S ratio.

Due to the additional uncertainty of the location and time of occurrence of the microearthquake sources, we treat the source parameters as unknowns and their initial locations and origin times as starting source parameters. For that, we apply a joint velocity-hypocenter inversion scheme (Lee and Stewart, 1981; Thurber, 1983). During each iteration of the inversion procedure, we calculate the updated V_P and V_P/V_S ratio models and use this information to recalculate the sources' hypocentral parameters.

An issue of using earthquake sources is that, in most cases, the medium is sampled unevenly and preferentially along certain directions defined by the seismicity rate of the study area as well as the location of active faults. As a result, the LET inverse problem is generally a mixture of over- and underdetermined problems and requires regularization to stabilize the inversion. This regularization is

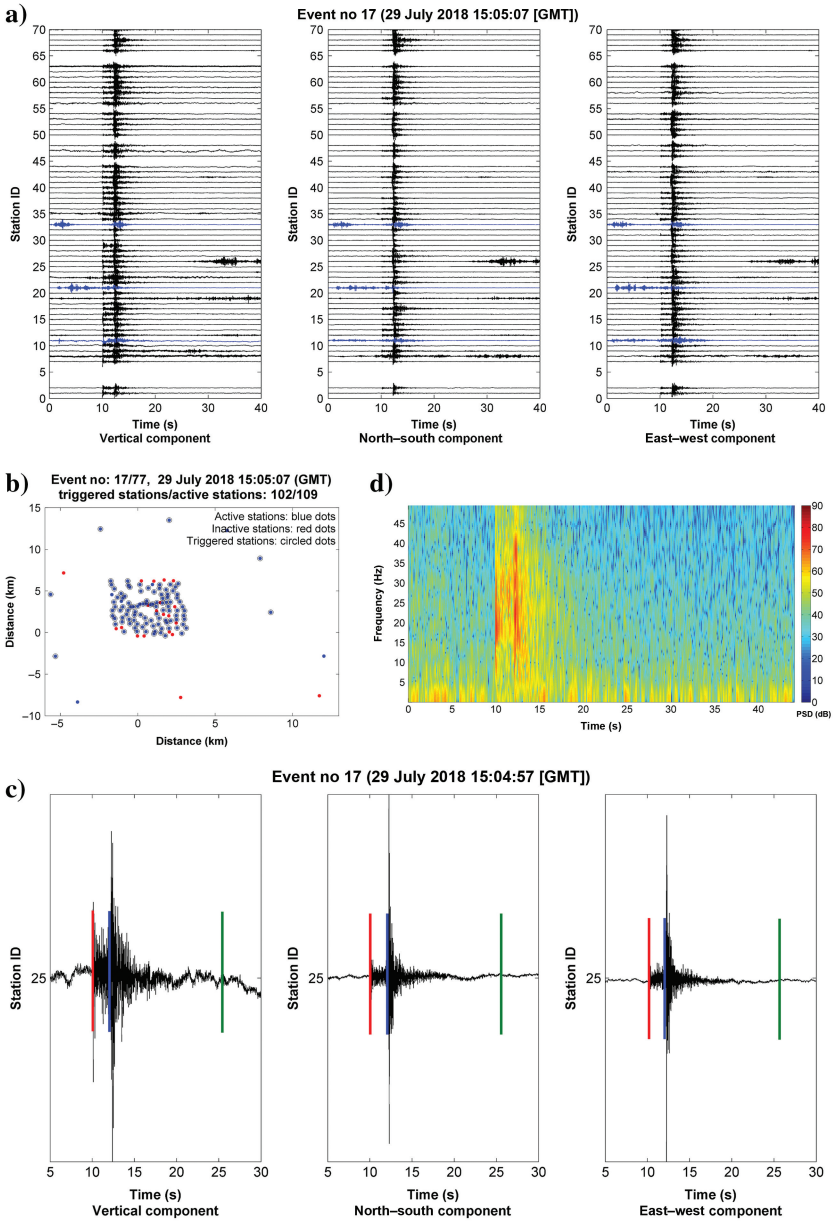

Figure 3. Data analysis procedure. (a) Event detection of the earthquake that occurred on the 29 July 2018 at 15:05:07 (GMT). Signals recorded by the three components of the first 70 stations of the Gerolekas seismic network (accepted traces in black and rejected traces in blue). (b) Locations of the triggered stations (circled blue dots) of the Gerolekas seismic network. (c) Picking of the first arrivals on the recordings of the three components of station 25 (red line: P-wave onset time, blue line: S-wave onset time, and green line: coda duration). (d) Spectrogram of the recording of the vertical component of station 25 presented in (c). PSD, power spectral density.

Downloaded 12/28/23 to 77.169.250.78. Redistribution subject to SEG license or copyright; see Terms of Use at http://library.seg.org/page/policies/terms
DOI:10.1190/geo2023-0213.1

done using an appropriate damping factor that controls the degree of parameter perturbations. We select the appropriate damping factor empirically, performing several single-iteration inversions for V_P and V_P/V_S ratio, through the construction of trade-off curves between the data and model variance, as proposed by Eberhart-Phillips (1986). The appropriate damping factor values are those that correspond to the best compromise between the data and model variance.

LET implementation

For the 848 selected microearthquakes, we obtained 98,763 exploitable P- and S-wave first arrivals (51,412 P-wave and 47,351 S-wave first arrivals), i.e., an average of approximately 117 first-arrival times per seismic event (61 P-wave and 56 S-wave arrival times). The high number of arrival times per earthquake, despite the very low magnitude of the exploited seismicity, is due to the very dense seismic network installed in the Gerolekas area and constitutes an indicator of the quality of the initial hypocenter-location solutions. In Table 1, we present a description of the inversion problem that we solve, in terms of number of known and unknown variables.

We perform LET using a revised version of the SIMULPS inversion code (Thurber, 1983; Evans et al., 1994). The inverse problem is solved using damped least squares based on singular value decomposition that incorporates a parameter-separation scheme between velocity and hypocenter parameters. Parameterization of the model space is achieved using the 3D grid-node technique, whereas the velocity values of the space between the model nodes are estimated using the linear B-spline interpolation. The forward problem is solved using the pseudobending approximation (Um and Thurber, 1987), which performs satisfactorily for ray lengths shorter than 80 km (Um and Thurber, 1987; Eberhart-Phillips, 1990), as in our case. In Figure 6, we present the raypaths involved in the inversion, along with the limits of the model space. We see that the ray coverage is excellent, especially for the inner model space, which constitutes the area of major interest.

We parameterize the model using different node distances for the inner (6 km × 8 km) and outer model space (see the rectangles in Figure 6). We use a finer grid of 500 m × 500 m for the inner model space, which delineates the actual area of interest, and a coarser grid of 1 km × 1 km for the remaining nodes. For depth parameterization, we also adopt a variable grid, setting a node every 500 m for the first 3.5 km from the surface (down to 2 km below MSL) and gradually increasing the internode distance down to the Moho (every kilometer down to 6 km below MSL, every 2 km down to 10 km, every 5 km down to 20 km, and a final node at 35 km). The vertical extent of the model space is defined by the depths of the hypocenters, located mainly shallower than 15 km with very few

Table 1. Number of knowns and unknowns that describe the Gerolekas inversion problem.

Knowns	P-wave observations	51,412
	S-wave observations	47,351
	Total	98,763
Unknowns	Model parameters for V_P $[x \times y \times z]$	11,339 [23 × 29 × 17]
	Model parameters for V_P/V_S $[x \times y \times z]$	11,339 [23 × 29 × 17]
	Hypocenter coordinates $[x \times y \times z]$	2544 [848 × 3]
	Origin times	848
	Total	26,070

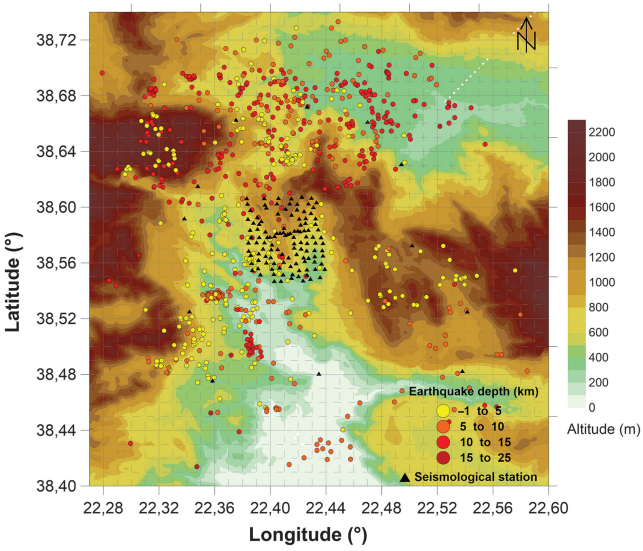

Figure 4. Spatial distribution of the Gerolekas seismicity. Color-coded dots correspond to the epicenters of the 848 selected microearthquakes that are used as the sources for the passive seismic methods. Their colors represent the earthquakes' depth of occurrence, whereas black triangles mark the locations of the 129 stand-alone seismological stations of the Gerolekas network.

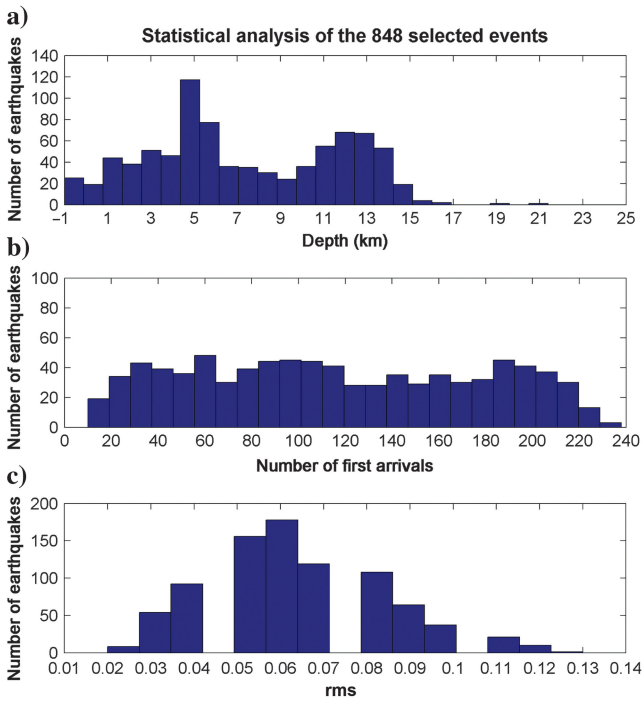

Figure 5. Statistical analysis of the Gerolekas selected 848 microearthquakes. Histograms showing (a) the occurrence-depth distribution, (b) the number of P- and S-wave first arrivals per microearthquake, and (c) the rms error of the earthquakes' locations.

Downloaded 12/28/23 to 77.169.250.78. Redistribution subject to SEG license or copyright; see Terms of Use at http://library.seg.org/page/policies/terms
DOI:10.1190/geo2023-0213.1

occurring at depths of approximately 25 km (histogram in Figure 3a), whereas the Moho depth in the area is expected at approximately 35 km (Sachpazi et al., 2007).

Due to the complexity of the structures and the exceptionally shallow depths that we aim to image, we perform a two-step 3D inversion procedure, with increasing complexity during each step. We initially invert only for V_P, using a simple 1D P-wave velocity model that has been estimated from the data by means of a rough initial 1D inversion of the coarse seismological model proposed by Latorre et al. (2004) for a nearby area, and a uniform V_P/V_S ratio of 1.78, estimated using the Wadati diagram presented in Polychronopoulou et al. (2020), as starting models. The 1D V_P starting model is presented in Table 2. We then repeat the procedure using the resulting output 3D V_P model as the starting model, along with the previously defined uniform V_P/V_S ratio and the relocated microearthquakes. In Figure 7, we present the trade-off curves for the Gerolekas data set. Regularization is done by selecting a damping factor equal to 10 for the V_P and the V_P/V_S inversion.

Inversion results

In Figures 8 and 9, we present the V_P and V_P/V_S ratio distributions, respectively, obtained from the field data along the depth slices of interest (from 500 m above MSL down to 2 km below MSL).

Examining the LET results, we can already extract some initial information on the subsurface below Gerolekas. For this, we focus on the unexplored part of the study area that is delineated by the surficial appearance of the Gerolekas nappe (brown lines in Figures 8 and 9) and compare them with the explored area around it. Taking into account the P-wave velocity distribution in Figure 8 and the known geology outside the Gerolekas nappe, we observe a clear separation between the flysch layer (V_P of the order of 4.0–4.5 km/s) and the underlying limestone of the normal Parnassus-Giona series (V_P higher than 4.8 km/s). This passage, which has already occurred at MSL for the northern part of the Gerolekas nappe and seems to be completed for almost all of the Gerolekas area at the depth slice of 500 m below MSL, is a first indicator that the geologic hypothesis of Figure 3b is not valid. This observation is of great interest for the mining potential of the Gerolekas area because the bauxite deposits are expected to reside slightly below this flysch-limestone interface. Moreover, the V_P/V_S ratio distribution in Figure 9 confirms this interpretation because it clearly shows a high V_P/V_S ratio area following the form of the surficial appearance of the Gerolekas nappe and extending down to depths between MSL and 500 m below MSL (V_P/V_S ratio values higher than 1.85). This can be explained by considering the V_S properties involved in the estimation of the V_P/V_S ratio because the formations of the overlap area are expected to be more disturbed than the same formations that appear in the neighboring tectonically stable areas, thus being characterized by lower V_S values. This is clear, especially for parts of the model space that are characterized by similar V_P and very different V_P/V_S ratio values. Consequently, a first evaluation of the Gerolekas LET results provides some insight into the depth at which the interface between the overlap formations and the formations of the normal Parnassus-Giona series lies — it begins a few hundreds of meters above MSL for the northern part of the Gerolekas nappe area and is completed a few hundreds of meters below MSL for the southern part. This information is directly linked to the exploration question that was initially set.

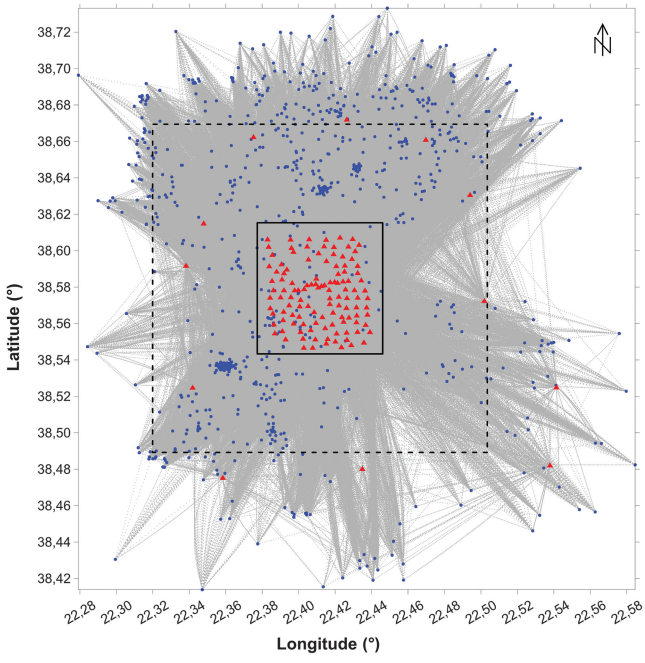

Figure 6. Raypaths used for the inversion of the Gerolekas data (gray lines). Red triangles represent the Gerolekas-network stations, blue dots represent the relocated epicenters of the 848 microearthquakes, the dashed black lines represent the model space, and the solid black lines represent the inner finely gridded model space corresponding to the area of interest.

Table 2. The V_P and V_P/V_S ratio starting models for the inversion.

V_P and V_P/V_S starting models		
Depth (km)	V_P (km/s)	V_P/V_S
1.5 (above MSL)	4.40	1.78
1.0 (above MSL)	4.60	
0.5 (above MSL)	4.80	
MSL	5.00	
0.5 (below MSL)	5.10	
1.0 (below MSL)	5.20	
1.5 (below MSL)	5.25	
2.0 (below MSL)	5.30	
3.0 (below MSL)	5.40	
4.0 (below MSL)	5.50	
5.0 (below MSL)	5.55	
6.0 (below MSL)	5.60	
8.0 (below MSL)	5.80	
10.0 (below MSL)	6.00	
15.0 (below MSL)	6.20	
20.0 (below MSL)	6.40	
35.0 (below MSL)	7.00	

The V_P model is estimated using a 1D inversion of the data, whereas the V_P/V_S ratio is estimated by means of a Wadati diagram (Polychronopoulou et al., 2020).

Downloaded 12/28/23 to 77.169.250.78. Redistribution subject to SEG license or copyright; see Terms of Use at http://library.seg.org/page/policies/terms
DOI:10.1190/geo2023-0213.1

Model robustness

The inversion resolution of LET is neither uniform nor fully controlled because it is heavily affected by the spatial distribution of the seismic rays spanning the study volume. Consequently, it is very important to accompany LET results with a means to assess the solution's quality at each part of the inverted volume. A detailed assessment of the Gerolekas LET model robustness is described in Appendix A.

TRANSIENT-SOURCE SI BY AUTOCORRELATION

The same 848 carefully selected local microearthquakes are further processed by the application of TSI by autocorrelation for retrieval of reflected waves.

According to the theory of seismic interferometry (SI), for a seismic station installed on the free surface above a horizontally layered subsurface and a source illuminating the target from below by a vertical plane wave, we can retrieve the global reflection response $R(t)$ that would be emitted from a virtual source co-located with the station under consideration and emitting energy vertically down. This is done by calculating the autocorrelation of the global transmission response $T(t)$ of the vertically propagating plane wave recorded at the free surface, corrected by a term corresponding to the pulse of the illuminating wavefield (the Kronecker $\delta(t)$) (Claerbout, 1968; Wapenaar et al., 2010):

$$R(t) + R(-t) = \delta(t) - T(t) * T(-t). \quad (1)$$

In the case of the Gerolekas data set, we apply this principle using the selected microearthquakes as sources, following the methodology proposed by Polychronopoulou et al. (2020). We select those of the 848 microearthquakes whose first arrivals are incident (nearly) vertically at a station of the Gerolekas seismic network. We assume that a recorded seismic ray is nearly vertical when the hypocentral location of an earthquake lies within a circular cone extending vertically down with its apex fixed on the station location and an apex half-angle equal to 20°. This is a prerequisite for the application of TSI by autocorrelation for reflected-wave retrieval, ensuring that the data satisfy the necessary condition of vertical illumination from below.

This procedure results in the selection of several microearthquakes whose first arrival is nearly vertical at a station of the Gerolekas network (Figure 10). These events will contribute to the retrieval of the zero-offset virtual reflection response below the station under consideration, by applying the processing steps described in Appendix B.

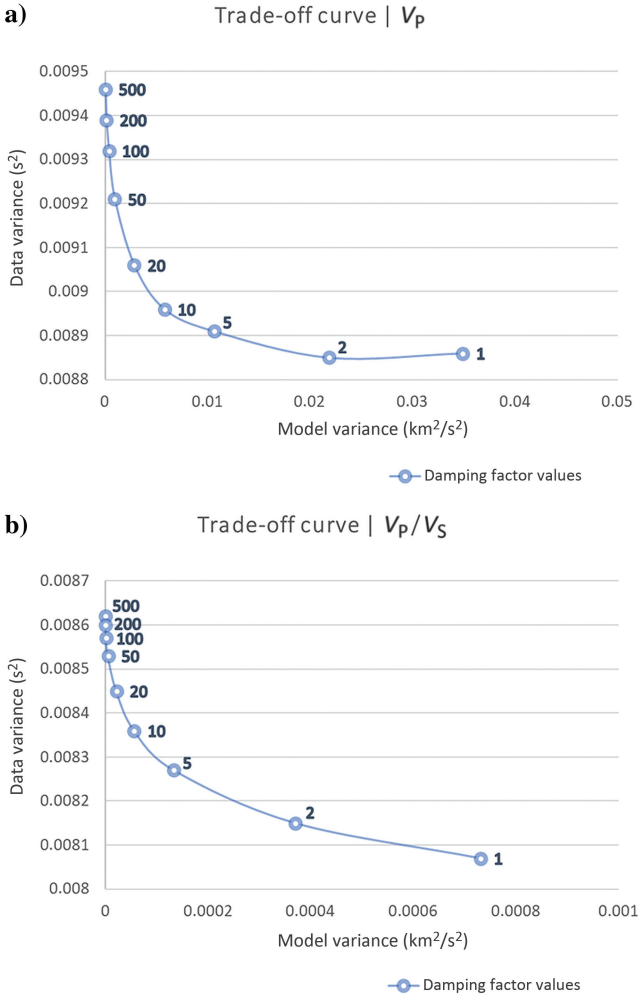

Figure 7. Model variance versus data variance for several single-iteration inversions: (a) for V_P and (b) for V_P/V_S ratio, using different damping factor values.

Weighted stacking

Unlike the simple stacking that was initially proposed in Polychronopoulou et al. (2020), we apply a two-step weighted summation procedure, taking into account the crosscorrelation coefficient (CCC) between the unstacked traces and a reference trace. This weighted-stacking procedure is a methodological addition that aims to improve the quality of the obtained virtual reflection responses below each station. We initially assess the overall quality of each trace, by building a reference trace per station and estimating the global CCC between each unstacked trace under investigation and this reference trace. The reference trace is the output of the simple stacking of all the traces that are obtained for a given station by the application of the processing sequence described in Appendix B. Traces that are characterized by insufficient correlation with the reference are discarded.

Following this, we calculate a new reference trace, by stacking only the traces that passed the correlation criterion of the previous step, to further assess these traces' quality. To make this assessment, we select an appropriate time window (in this case we select a window length of 10 samples) and estimate the local CCC with the new reference trace for each part of the unstacked traces. This provides a means of assessing the traces' local coherency and serves as a weighting factor that highlights the coherent parts, where the estimated CCC lies above a specific threshold value (in this case set at 50%), whereas it suppresses the noisy parts of the obtained signal, for which CCC is either lower than the threshold value (incoherent parts) or negative (coherent but of opposite polarity). The resulting weighted traces are then stacked per station and component, and the remaining reflectors are kept only if they are observed in several unstacked traces (in this case more than five). The obtained final summed results at each station correspond to the retrieved zero-offset virtual reflection response that would be acquired if a source and

Downloaded 12/28/23 to 77.169.250.78. Redistribution subject to SEG license or copyright; see Terms of Use at http://library.seg.org/page/policies/terms
DOI:10.1190/geo2023-0213.1

a receiver are colocated at the station's location and the source is emitting energy vertically down.

An example of the application of the weighted-stacking procedure on the signals recorded by station 118 of the Gerolekas seismic network is shown in Figure 11. We select station 118 for two reasons: (1) it is located at the edges of the network and thus provides the opportunity to check if the limited azimuthal coverage of such location affects SI results and (2) it is located close to mining waste piles, where material is occasionally dumped, affecting local noise conditions. Observing the stacked ACF resulting at each step of the procedure, we note that the obtained final stacked traces (right panels in Figure 11) are globally similar and we delineate areas where the weighted-stacking procedure suppresses incoherent parts of the ACFs, providing a less noisy image (red rectangles in Figure 11). For example, the reflector R1 in Figure 11c (at approximately 90 ms) is enhanced because the procedure eliminates the few traces that remained locally incoherent, even after discarding the globally incoherent traces (Figure 11a and 11b). In contrast, the area at approximately 450 ms (R3), where two small reflectors appear as a result of stacking visibly incoherent signals, is improved in Figure 11c, in which their amplitudes are further reduced. Another difference is observed at approximately 240 ms (R2), where we observe two reflectors clearly separated before local weighting (Figure 11a and 11b), which tend to merge in one in Figure 11c.

The low CCC that characterizes the discarded traces can be explained either by their severe contamination by noise — due to variable local noise conditions that occasionally affect the recorded signals at a specific station — or by some violation of the stationary-phase region of vertical incidence that is assumed. This violation might be due to an erroneous selection of the condition of near-vertical incidence (if the assumed incidence angle is larger than it should be) or to significant error at the relevant hypocentral location that may be placing an earthquake inside the selected zone, whereas, in reality,

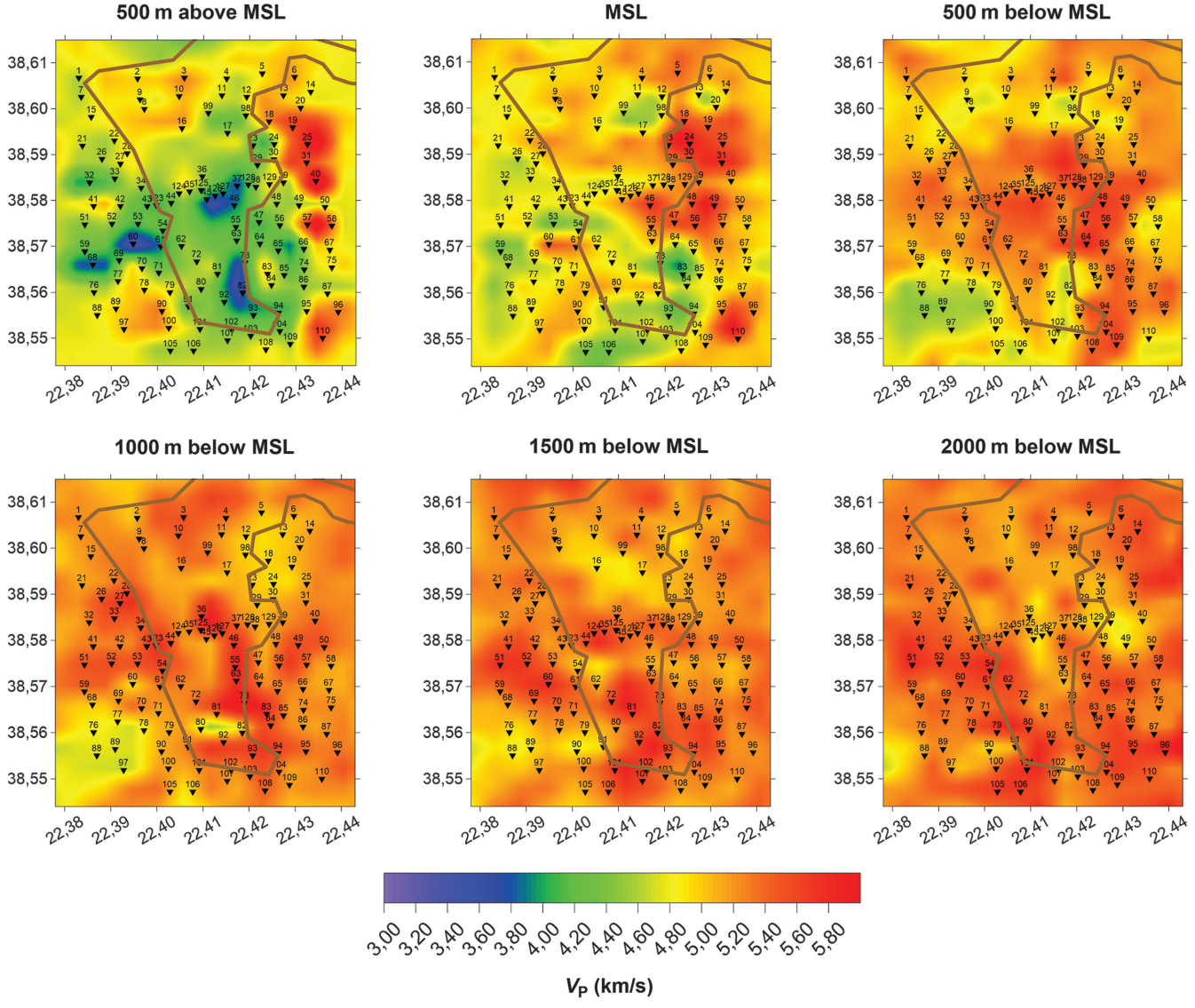

Figure 8. The P-wave velocity distribution along depth slices crossing the study area. The depth slices range from 500 m above MSL to 2 km below MSL. Black triangles represent the Gerolekas-network stations, and brown line represents the superficial appearance of the Gerolekas nappe.

it is located outside. To examine this, we depict the selected events, satisfying the verticality criterion that was set, below station 118 and show which of these events are rejected during the first step of the weighted-stacking procedure (Figure 12). We see that the spatial distribution of the rejected earthquakes is random and they are not located at places that would imply either a problematic selection of the stationary-phase region (e.g., if they were located at the edges of the cone of Figure 12) or significant error at their hypocentral location (e.g., if they were located at the poorly azimuthally covered area at the north, northwest of station 118). Consequently, we consider that the low correlation of specific traces is most probably due to increased local noise levels at specific times.

TSI results

We further process these traces by applying standard seismic-exploration processing routines to obtain zero-offset seismic sections along directions of interest. For that, we use CWP/SU: Seismic Un*x (Cohen and Stockwell, 2008). We apply static corrections, taking into account the significant elevation differences of the Gerolekas site (elevations range between 300 m and 1300 m above MSL for an area of 5 km × 7 km) and time-to-depth conversion to the resulting time sections, using an average 1D P-wave velocity model (estimated from LET).

In Figure 13, we present the obtained virtual zero-offset reflection responses by the application of TSI by autocorrelation on the signals recorded by the vertical component of the stations along the TSI profile 01-106, using the proposed weighted-stacking procedure (Figure 13a) and the simple stacking that was initially applied (Figure 13b). The presented depth sections provide information from the surface (elevations that range between 300 m and 1000 m) down to a depth of 2 km below MSL. Note that the zero-offset traces are interpolated for visualization purposes. This profile is selected because part of it follows one (PARV-3) of the three 2D active-source seismic profiles acquired in 2003 along the edges of the Gerolekas overlap area. Locations of the TSI profile 01-106 as well as the 2D active-source seismic profiles PARV-1, PARV-2, and PARV-3 are shown in Figure 1.

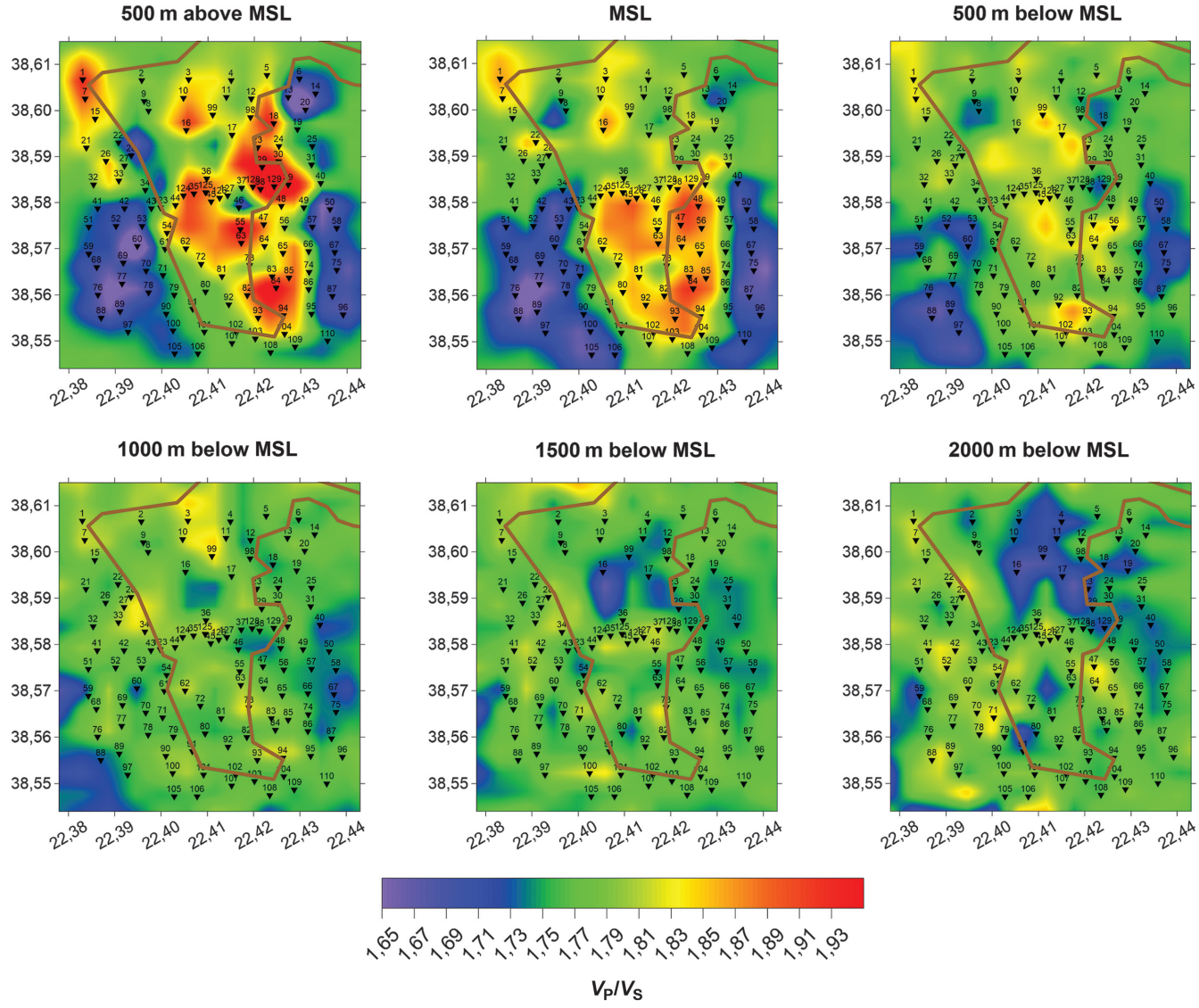

Figure 9. As shown in Figure 8 but for the V_P/V_S ratio.

Downloaded 12/28/23 to 77.169.250.78. Redistribution subject to SEG license or copyright; see Terms of Use at http://library.seg.org/page/policies/terms
DOI:10.1190/geo2023-0213.1

Downloaded 12/28/23 to 77.169.250.78. Redistribution subject to SEG license or copyright; see Terms of Use at http://library.seg.org/page/policies/terms
DOI:10.1190/geo2023-0213.1

LEGACY SEISMIC DATA

In 2003, active seismic data were acquired in the Gerolekas area, along three seismic profiles (PARV-1, PARV-2, and PARV-3), by Hellenic Petroleum (Figure 1). In 2004, Hellenic Petroleum processed the seismic data up to poststack time/poststack depth migration. Original processing and interpretation results were available only as hardcopies (for an original processing example, see Polychronopoulou et al., 2020). During the original processing, only the field statics were applied, using a datum of 800 m and a replacement velocity of 3500 m/s. All profiles were acquired using vibroseis (15–90 Hz sweep, five sweeps/vibroseis point). Acquisition parameters for each line are summarized in Table 3.

Seismic data reprocessing

Original data are initially inspected for bad or test shots and merged into shot gathers for each line (2 s long, with a sampling of 2 ms). Lines PARV-2 and PARV-3 partially overlap, but due to their different receiver spacing, they are processed separately. During the reprocessing, a crooked line geometry is adopted for each profile, with the following bin sizes: PARV-1, 7.5 m; PARV-2, 5 m; and PARV-3, 2.5 m. We use the same replacement velocity (3500 m/s) that was used during the original processing. The basic processing flow is summarized in Table 4.

On average, the data quality was good. An example shot gather before and after processing is shown in Figure 14. There is a strong effect of topography, which is visible in the shape of the first arrivals. Reflections are discontinuous in general, but there are energetic wide-angle reflections present, originating from a high-velocity layer. The presence of this layer was causing problems during velocity analysis and required a careful mute-function design. Therefore, in the next steps, prestack depth migration (PreSDM) is attempted for all the profiles.

During the reprocessing, a lot of attention was paid to the statics. We test refraction statics and tomostatics, concluding that the tomostatics provide a better reflection alignment.

Depth imaging

Due to the presence of strong lateral and vertical velocity contrasts, in the next step we run PreSDM for all of the profiles. We start with the PARV-1 profile, in which long offsets (up to 5 km) are present. First-arrival energy is picked up to the farthest offset and first-arrival tomography (FAT) is applied (Zhang and Nafi Toksöz, 1998), using the full-offset range, to produce a starting velocity model for migration. However, due to the presence of shadow zones and complex wavefields, picking of first arrivals is very tedious.

Because of the preceding, we make use of the passive seismic velocity model estimated by LET, as an alternative velocity model for PreSDM. Smooth velocity distributions are extracted from the 3D LET results along the seismic profiles and regridded to match the common-depth points spacing. Subsequently, we perform standard Kirchhoff PreSDM. Figure 15 shows a comparison of the depth-migrated stacks along the seismic line PARV-1, obtained using the FAT and LET models, respectively.

Note that the LET velocities seem to be more conformable with the general structural pattern, whereas velocity values of the LET model seem to be lower beneath the depth of 750–1000 m (below the seismic datum). The final PreSDM stack reflectors of Figure 15b are flatter and a shallow reflector (undetectable in Figure 15a) appears at a depth of approximately 250 m (below the datum) between the common-depth points of 110 and 150. This also is reflected in the common-image gathers, which are clearly showing flatter events for the migration using the LET model (Figure 16). This can be explained by the fact that the LET velocity distribution is more robust, especially at greater depths, than the respective FAT model. In addition, the FAT velocity model is built using near-horizontally propagating refracted arrivals, whereas in the LET model, the dominant rays are more vertical and therefore more compatible with near-vertical incidence reflection data.

Based on the comparison of the results of PreSDM along PARV-1, we decide to use the LET-derived velocity model for migrating the other two profiles. After inspection of the common-image gathers, the LET velocities are scaled by 85% for migrating lines PARV-2 and PARV-3 because this seems to provide the optimum migration results. The need to downscale the LET velocities shows that the LET velocity field is probably overestimated along the seismic profiles. This could be due to two possible reasons: (1) an erroneous selection of an overestimated starting velocity model for the LET inversion and (2) the fact that the values of the LET velocity model are estimated for large volumes (LET grid of 500 m × 500 m × 500 m), which might result in overestimating the values close to the surface.

INTERPRETATION

To exploit the results of the Gerolekas passive seismic survey better, we need to calibrate them using the available geologic knowledge, which is mainly based on well information from the numerous wells drilled in the surrounding area. These wells, despite being very shallow and located outside the Gerolekas overlap area, provide a robust means of evaluating our results and serve as control points in our attempt to correlate geophysical images with geologic formations. This correlation was one of the reasons why we designed a

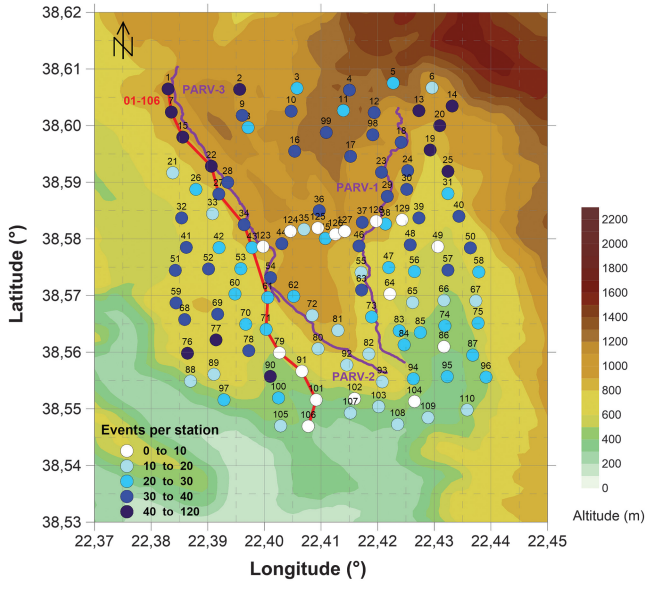

Figure 10. Number of events satisfying the verticality criterion at each station of the Gerolekas inner network. Red line represents the location of the TSI profile 01-106, and magenta lines represent the active-source seismic profiles PARV-1, PARV-2, and PARV-3.

Downloaded 12/28/23 to 77.169.250.78. Redistribution subject to SEG license or copyright; see Terms of Use at http://library.seg.org/page/policies/terms
DOI:10.1190/geo2023-0213.1

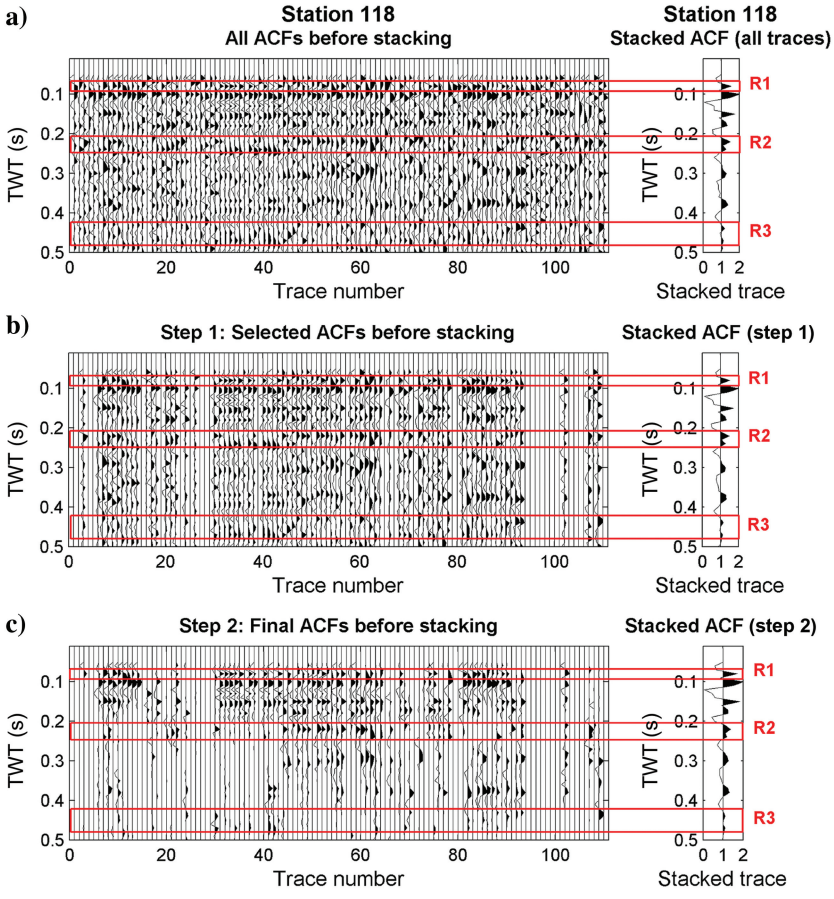

Figure 11. Weighted-stacking procedure applied on data recorded by the vertical component of station 118 of the Gerolekas seismic network. (a) Unstacked ACFs of all the signals (left) and initial reference trace (right). (b) Selected ACFs by means of assessing the global CCC per trace with the initial reference trace (left) and intermediate reference trace calculated by summation of the selected traces (right). (c) Selected parts of the ACFs by means of assessing the local CCC per time window with the relevant part of the intermediate reference trace (left) and final reference trace (right). The red rectangles delineate areas where improvement is observed.

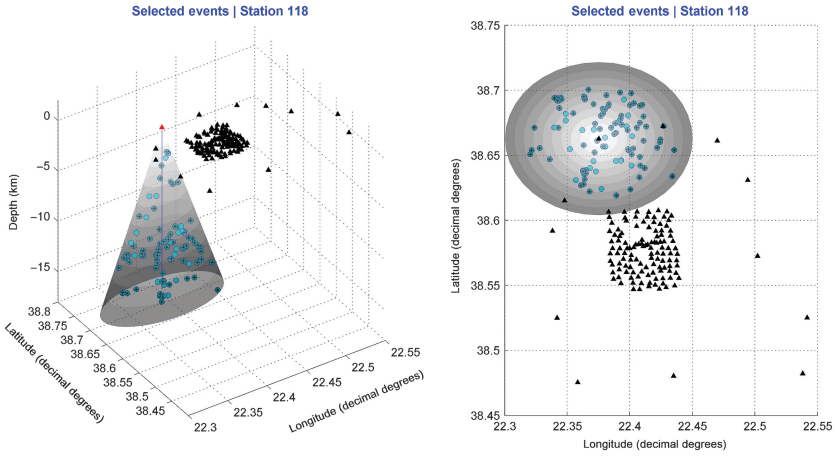

Figure 12. The assumed stationary-phase region of near-vertical incidence below station 118 of the Gerolekas seismic network (gray cone). Black triangles represent the 129 stand-alone seismological stations of the network, red triangle represents the station 118, cyan circles represent the selected events with hypocenters inside the stationary-phase region, and asterisks represent those of the selected events that are accepted by the weighted-stacking procedure.

seismic network spanning a broader area that also includes parts of the mining site that are thoroughly explored. This also is the reason why we select to focus our interpretation on TSI profile 01-106 — it follows PARV-3, which is the only active-source seismic line that is located relatively close to several the existing wells (see Figure 1), thus providing the opportunity to jointly evaluate active- and passive-source seismic data with geologic information.

We select those of the wells that are located along the TSI profile 01-106 (Figure 1) and present their findings in Figure 17a. The geologic formations encountered during drilling are flysch, different types of limestone, as well as rare and mainly superficial appearances of alluvia. The places where bauxite is drilled are marked with the red crosses on the relevant wells because the thickness of the bauxitic lenses is too small to be depicted along the TSI profile. We overlay well data on the reprocessed active-source seismic line PARV-3. Even though PARV-3 is located at a relatively short distance from the selected wells, we observe a good correlation between the reflectors that appear at a depth of approximately 600 m above MSL (offsets: 200–1400 m and 3400–4200 m) with the flysch-limestone interface that is observed in the well data.

Following this, we examine the imaged reflection responses on TSI profile 01-106, searching for reflectors with similar characteristics, to delineate the geologic interfaces in the subsurface. We then evaluate the detected interfaces, taking into account the well information along the profile, and we attribute them to specific geologic formations. These interfaces, corresponding to the bottom of the different layers, are shown in Figure 17b. More specifically, dashed green and blue lines correspond to the bottom of flysch and limestone, respectively, whereas the gray lines delineate areas where the virtual reflectors seem to be interrupted and are interpreted as faulting zones. We overlay the SI data, along with their interpretation, on the active-source data of Figure 17a, and we observe a satisfactory correlation between active- and passive-source reflectors. We note that the location of the areas interpreted as faulting zones is confirmed by the reprocessed active-source data because the relatively continuous reflectors that appear at the beginning of PARV-3 are interrupted and become chaotic between the offsets of approximately 1500 m and 3000 m.

The imaging capacity of the application of the TSI methodology in the case of the Gerolekas data set does not permit the delineation of layers thinner than approximately 50 m because the average frequency of 25 Hz that is observed in the P-wave coda of the recorded earthquakes, along with the average P-wave velocity of

Downloaded 12/28/23 to 77.169.250.78. Redistribution subject to SEG license or copyright; see Terms of Use at http://library.seg.org/page/policies/terms
DOI:10.1190/geo2023-0213.1

4–5 km/s, results in vertical seismic resolution on the order of 40–50 m (λ_{min} = 160–200 m and $\lambda/4$ = 40–50 m). As a result, we cannot interpret bauxitic lenses. Instead, we aim to delineate areas where bauxite is more likely to exist by considering that the bauxitic lenses in the surrounding area are located close (right below) to a flysch-limestone interface as well as considering the well data. In any case, the major target of this survey is to evaluate the hypotheses assumed for the flysch-limestone interface below the Gerolekas overlap (Figure 2).

Depending on the polarity of the virtual reflectors forming each delineated interface, we draw conclusions about the characteristics of the two layers forming the interface in terms of the impedance contrast. Equation 1 shows that the autocorrelated transmission response should be multiplied by −1 to retrieve a positive reflection response. As we do this, a passage to a layer of higher velocity and density will be marked by virtual reflectors with a positive polarity, whereas a passage to a layer of lower velocity and density will be marked by a negative polarity. In the case of the Gerolekas survey, we expect the flysch layer to be characterized by lower seismic velocity and density than the different types of limestone. More specifically, according to Orfanos et al. (2021), an average value of the P-wave velocity (V) and the density (ρ) of the flysch and limestone formations that appear in the Gerolekas area have been estimated, using in situ measurements inside the mine's galleries, as well as laboratory measurements of core samples. These average values are: V_{flysch} = 3.1 km/s, ρ_{flysch} = 2.61 g/cm^3, $V_{limestone}$ = 4.5–4.8 km/s, and $\rho_{limestone}$ = 2.67–2.71 g/cm^3. Because the geology of the study area is quite complicated, we expect velocity inversions, due to the Gerolekas stratigraphic overlap. These velocity inversions, which in the case of TSI profile 01-106 are interpreted as passage from a limestone to a flysch layer, appear on the zero-offset virtual reflection profile as reflectors of negative polarity that delineate the interface between the two different lithologies (e.g., interface at a depth of approximately 500–560 m above MSL for the first 1300 m of the profile; interface at 380–440 m above MSL for distances of 1700–2600 m; and interface at 290–310 m above MSL for distances of 3900–6000 m).

Finally, to evaluate our results, we superimpose the interpreted interfaces on the well data of Figure 17a. Observing Figure 17c, we see that the top flysch layer, which is delineated in detail by well data, is reconstructed quite well by the virtual reflectors obtained using TSI by autocorrelation. It is followed by a limestone layer, hosting bauxitic lenses close to the flysch-limestone interface for the major part of TSI profile 01-106. However, this is not the case for the part of the

Table 3. Acquisition parameters for the legacy active seismic lines PARV-1, PARV-2, and PARV-3.

	Acquisition parameters		
	PARV-1	PARV-2	PARV-3
Receiver interval (m)	15	10	5
Shot interval (m)	15	10	5
Active channels	360	220	200
Max offset (m)	5377.5	2295	1992.5

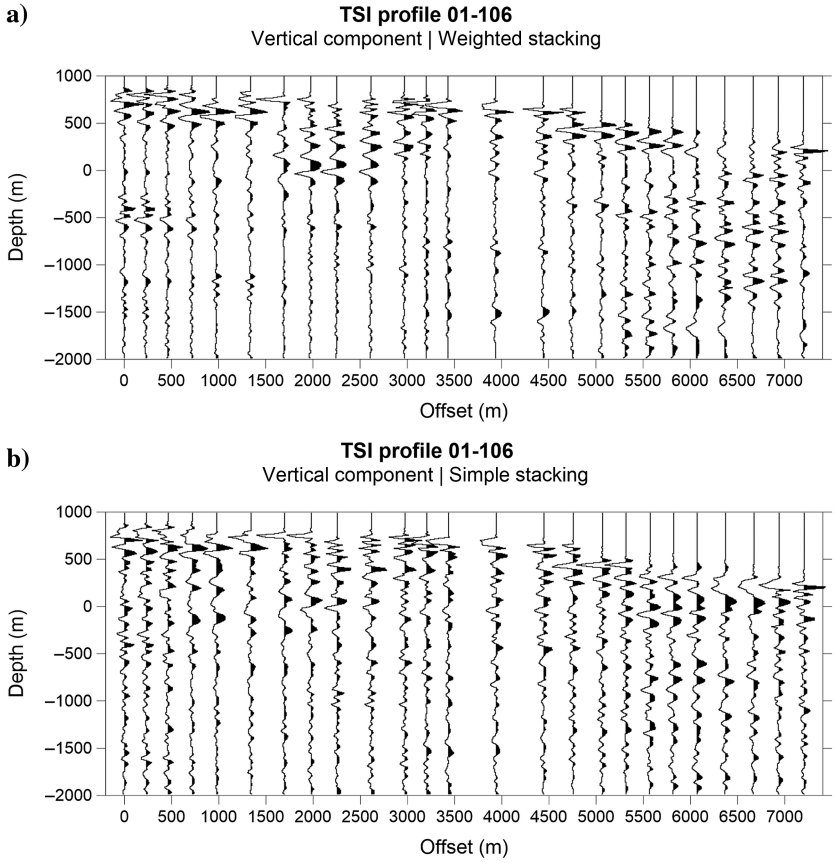

Figure 13. Virtual reflection zero-offset depth sections along the TSI profile 01-106, part of which follows the active-source seismic line PARV-3 from Figure 1. The depth sections are obtained by the application of TSI by autocorrelation using P-wave coda, and using the (a) weighted-stacking and (b) simple-stacking procedure.

Downloaded 12/28/23 to 77.169.250.78. Redistribution subject to SEG license or copyright; see Terms of Use at http://library.seg.org/page/policies/terms
DOI:10.1190/geo2023-0213.1

profile between distances of 1500 m and 3500 m, where two faulting zones seem to be heavily affecting the subsurface. At this part of the profile, bauxite is found close to the second flysch-limestone interface, which is located after the flysch reappearance, at a depth of approximately 250 m above MSL.

This observation can be directly linked to the stratigraphic overlap of the Gerolekas area because the TSI profile 01-106 is located at the edges of the Gerolekas nappe. Figure 18 depicts the LET V_S distribution at the depth slice of 500 m above MSL and shows that the affected part of the profile (purple ellipse in Figure 18) is located along a discontinuity separating the Gerolekas overlap from the surrounding areas. We choose to plot V_S because we expect to encounter the same formations (flysch and limestone) but affected by different degrees of disturbance (due to faulting), rather than different formations. We use the velocity distribution of Figure 18 to delineate areas with similar characteristics with the various zones of interest that appear along the TSI profile. We jointly evaluate the findings of Figures 17 and 18 and conclude that for the areas located at the west of the purple ellipse, possible bauxite deposits are probably located below the first flysch-limestone interface, whereas toward the east (below the Gerolekas overlap), they should be expected deeper, after the flysch reappearance.

Consequently, for the part of the profile that belongs to the overlap area, TSI findings show that the flysch-limestone interface of interest is located at a depth of 250 m above MSL, thus confirming the geologic hypotheses in Figure 2c or 2d. The scenario in Figure 2b, which assumes that this interface has been moved to several hundreds of meters below MSL and possible bauxite deposits are of no mining interest, is clearly rejected. Moreover, using the LET S-wave velocity distribution, we show that the findings of the well 3487 in Figure 17, which is drilled at the edges of the Gerolekas overlap area and finds bauxite at the depth of 200 m above MSL, conform with the geology below the disturbed area. Taking into account the fact that the type of the bauxite deposits found by this well are similar to the ones encountered in the surrounding area, we conclude that the prevailing hypothesis for the subsurface below Gerolekas is the one shown in Figure 2c.

Table 4. Reprocessing workflow for the Gerolekas data.

Reprocessing workflow	
1	Read SEG-Y
2	Geometry merge
3	Spherical divergence compensation (t_{pow} = 1.2)
4	Tomostatics
5	Floating datum correction
6	Air wave attenuation
7	Velocity steered median filter (V = 1000, 1500 m/s) applied to a cone defined by V = 1500 m/s
8	*f-x* deconvolution
9	Trace edits
10	Surface-consistent spiking deconvolution (150 ms operator)
11	Single-trace predictive deconvolution (150 ms operator, 12 ms gap)
12	Band-pass filtering (18–22–80–90 Hz)
13	Automatic gain control (500 ms)

DISCUSSION

In the case of the Gerolekas mining investigation, the main challenge related to the application of LET was the fact that even the indirect exploration target (flysch-limestone interface) was expected

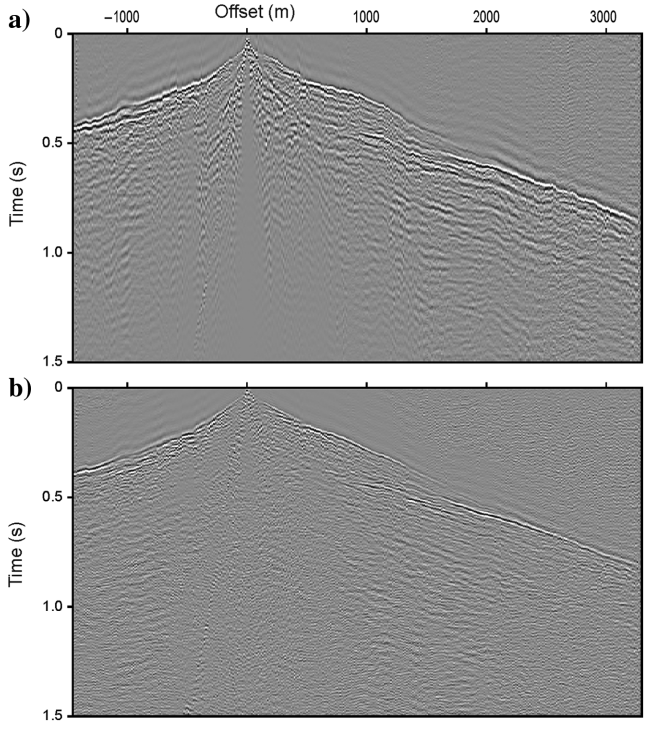

Figure 14. Example of shot gather from PARV-1 profile: (a) raw data and (b) processed data.

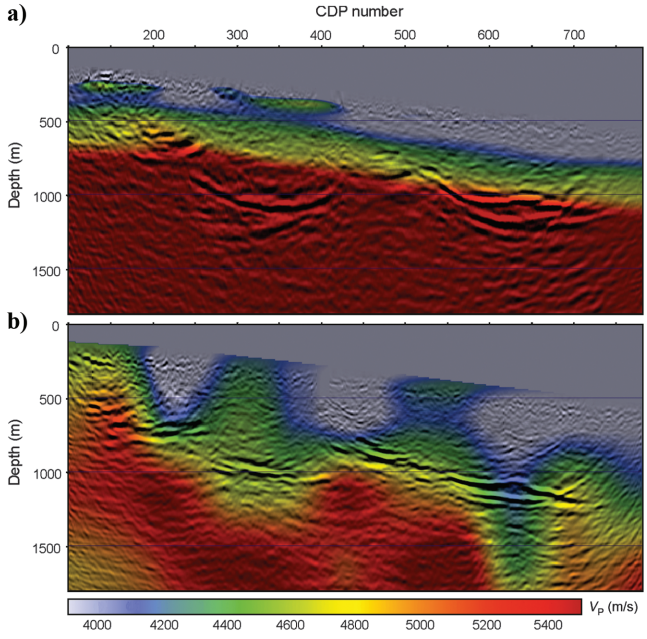

Figure 15. Final PreSDM stacks along the line PARV-1. The stacks are obtained using (a) FAT and (b) LET velocity models (overlain in the background).

Downloaded 12/28/23 to 77.169.250.78. Redistribution subject to SEG license or copyright; see Terms of Use at http://library.seg.org/page/policies/terms
DOI:10.1190/geo2023-0213.1

to lie at relatively shallow depths (less than 1 km below the surface), which constitutes the weaker zone for LET imaging. To overcome this, we exploited very small-magnitude local microearthquakes, occurring at shallow depths, along with a dense network recording at the surface. This resulted in a satisfactory coverage of the upper part of the study area with seismic rays, traveling at various directions, as we confirmed by the model robustness assessment that we performed.

From the two factors that affected the method's capability to image such shallow depths (dense network and shallow microearthquakes), only the network is controllable. The exact number and depth of occurrence of the earthquake sources are unknown before data analysis and only assumptions can be made, based on the area's regional seismicity. However, the Gerolekas experiment shows that in seismically active areas, such as Greece, low-magnitude events, which are usually not recorded by global or regional networks (because they can only be recorded at limited distances from their epicenters), are always present and the operation of a very dense seismological network at the surface is necessary to reveal their existence.

Our results show that LET provided a means of distinguishing between different formations (e.g., flysch and limestone), using the P-wave velocity, and also of delineating areas where the same formation is more disturbed due to the overlap faulting (e.g., limestone of the overlap compared with limestones of the normal Parnassus-Giona series), using the V_P/V_S ratio distribution. In contrast, the LET results suffer from relatively low resolution, taking into account the scale of the survey. Consequently, the LET output only provides a coarse estimation of the zone where the flysch-limestone interface is expected below the Gerolekas nappe (somewhere between 500 m above and below MSL). Given the abundance of microseismicity in the area, LET results could be further improved with the installation of a denser seismic network.

We improved autocorrelation-based TSI imaging by applying a weighted-stacking procedure, based on the estimation of the CCC (global and local) between each unstacked trace and a reference virtual reflection response below the station under consideration. This procedure provided a means of eliminating incoherent signals (or at least decreasing their amplitudes), which seemed to be affecting the retrieved virtual reflection responses, even after application of a simple-stacking procedure. We analyzed the location of the rejected traces and confirmed the correct selection of the stationary-phase region of vertical incidence. Consequently, we verified that the retrieved virtual reflection responses do not suffer from mode conversion contamination, due to the accurate estimation of the sources' locations and the strict selection of events occurring inside the stationary-phase region for each station. Note that the nature of the signal used — the P-wave coda of local microearthquakes — ensures that our signals are not affected by surface waves or near-surface effects. We explained the existence of incoherent signals after simple stacking as the result of variable local noise conditions at the recording sites, which is very common in areas with mining activity. During the month-long continuous data acquisition, repetitive noisy works take place at different locations of the mining site, affecting some of the recorded signals. Our results show that an assessment of each signal's quality before stacking and a weighted contribution of each trace, based on its coherency, provides a clearer imaging of the subsurface.

We exploited the obtained passive seismic results in two ways. We initially used them for reprocessing legacy active seismic data that were acquired in the area and originally processed in 2004. We reprocessed the original data and performed PreSDM using the FAT- and LET-derived velocity models. Comparison between the obtained PreSDM stacks shows that migration using the LET model results in the obtaining of flatter events and the appearance of hidden reflectors (see Figure 15). The relatively coarse (compared to active seismic) velocity model of LET provides a more robust image, especially for the deeper parts of the seismic profile, for which FAT suffers due to the ray penetration (ray channeling along high-velocity anomalies) and the presence of velocity inversions. Due to the nature of the earthquake sources, which illuminate the model space from below, LET is less affected by signal-penetration issues, whereas the 3D nature of the LET model provides a means of considering the 3D effect, especially in cases of complex geologic settings and crooked-line acquisition. Moreover, the refracted arrivals used for FAT are more sensitive to horizontal velocities, thus less compatible with the near-vertical incidence reflections. Compared with that, LET uses vertical raypaths from the earthquakes below the target, which are better suited for imaging near-vertical incidence data. A single

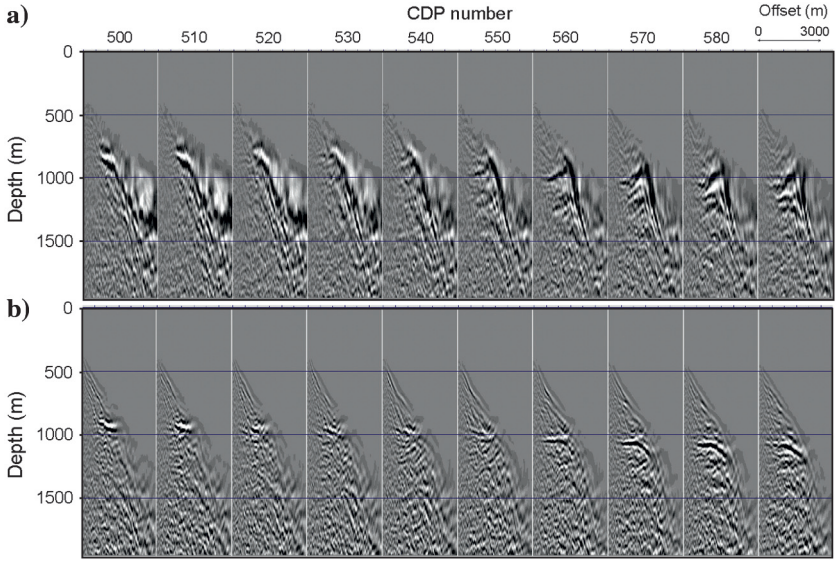

Figure 16. Common-image gathers obtained after migrating PARV-1 data using (a) FAT and (b) LET velocities.

Downloaded 12/28/23 to 77.169.250.78. Redistribution subject to SEG license or copyright; see Terms of Use at http://library.seg.org/page/policies/terms
DOI:10.1190/geo2023-0213.1

scaling factor (85% in the case of line PARV-3) applied to the LET velocity model was sufficient to produce consistently flat gathers across almost the whole profile. These results can be further improved by updating the velocity model using reflection tomography. In this case, the LET model will serve as a more robust starting model than the one typically derived by converting the stacking/prestack time migration velocities to interval velocities.

Following this, we attempted to jointly interpret the obtained passive seismic results. For that, we selected a profile that is affected by the Gerolekas overlap and, at the same time, passes through an area where active-source seismic and well data are available, for calibration and evaluation purposes. Unlike the LET results, TSI by autocorrelation provided virtual reflection imaging with a minimum resolution on the order of 40–50 m. This discriminating capacity, which is difficult to achieve with an earthquake-based survey — where the involved signals are of lower frequency than in the case of active-source seismic surveys — proved to be adequate for the delineation of the target of this mining exploration study. Interpretation of the retrieved virtual reflectors along the TSI profile 01-106 provided an insight on the subsurface, despite the complex geologic setting (faulting zones, stratigraphic inversions, etc.). We showed that the part of the TSI profile for which well data are available correlates satisfactorily with the well information, whereas this information is used to assign the interpreted reflectors to specific geologic formations. Moreover, we confirmed the presence of some of the interpreted features — faulting zones and flysch-limestone interfaces — in the reprocessed final PreSDM stack along the active-source seismic profile PARV-3. We jointly interpreted the obtained results and estimated the depth at which the interface of interest lies along the examined profile, thus evaluating the existing geologic hypotheses for the subsurface below Gerolekas. We concluded that the prevailing scenario is the one described in Figure 2c, which assumes that the targeted flysch-limestone interface is located at a depth close to MSL — at approximately 250 m above MSL along the TSI profile 01-106 — and followed by bauxite deposits similar to those of the surrounding area. These observations were further extended in space using the velocity distribution from LET.

It must be noted here that our work is a first step toward integrating a purely earthquake-based approach in mineral exploration. Even though the results are encouraging, it is evident that they could be further improved with a denser coverage of the study area with seismological stations. This would improve the spatial resolution of LET and TSI by autocorrelation and, with the selection of interstation distances adequate for crosscorrelating the signals without introducing any aliasing effects, it would even permit 2D/3D TSI processing. Finally, exploitation of the S-wave virtual reflection responses from the horizontal components of the recording passive seismic stations could further contribute to the illumination of the subsurface below the study area.

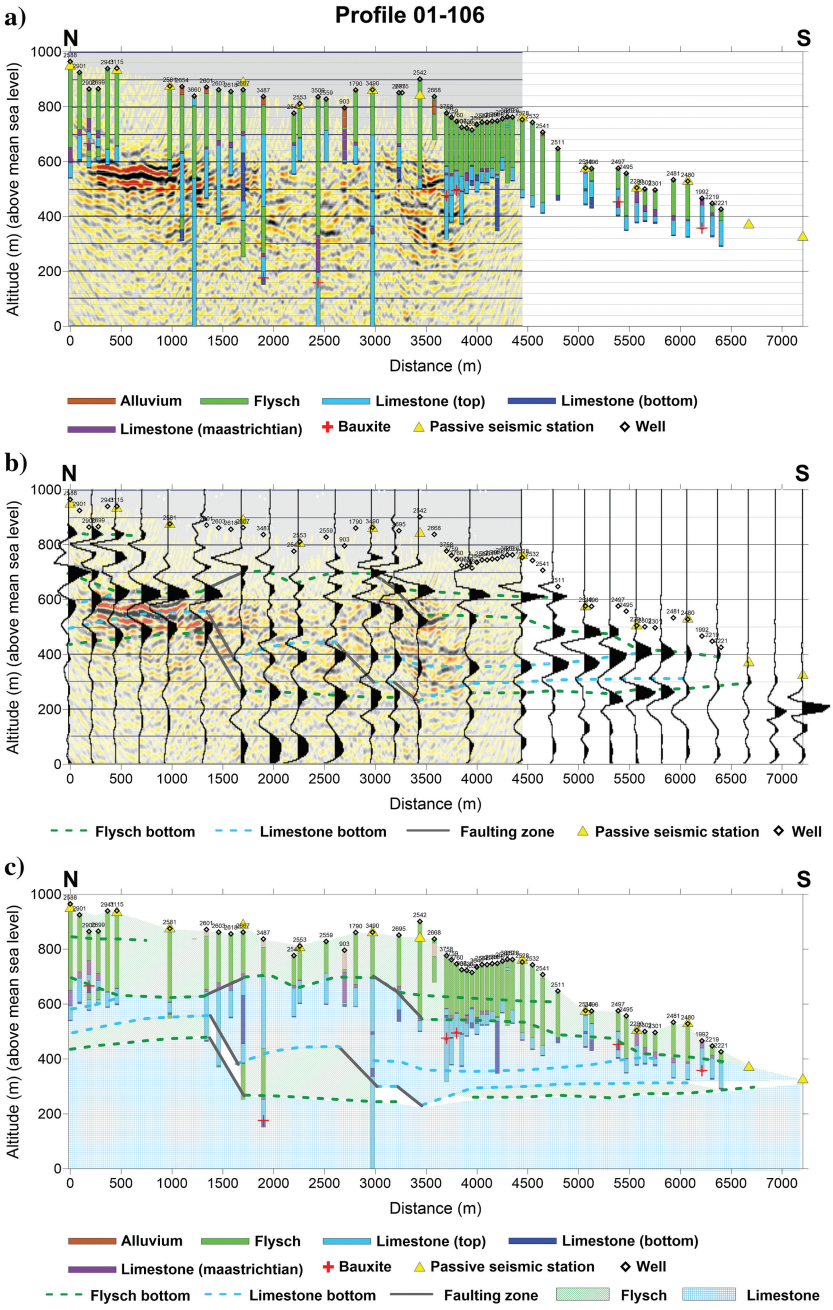

Figure 17. (a) Available well data along TSI profile 01-106 overlain on the final PreSDM stack along the active-source seismic line PARV-3. The stack is obtained using the LET velocity model. (b) Interpretation of the virtual reflection zero-offset depth section along TSI profile 01-106 obtained from TSI by autocorrelation using P-wave coda and the weighted-stacking procedure. Dashed lines correspond to the estimated bottom of the different layers, whereas gray lines denote the location of faulting zones. The TSI profile is overlain on the active-source final stack of (a). (c) The interpretation of TSI profile 01-106 superimposed on the available well data. For all three panels, well locations are marked with the black-outline rhombi, whereas Gerolekas-network stations are indicated by the yellow triangles.

Downloaded 12/28/23 to 77.169.250.78. Redistribution subject to SEG license or copyright; see Terms of Use at http://library.seg.org/page/policies/terms
DOI:10.1190/geo2023-0213.1

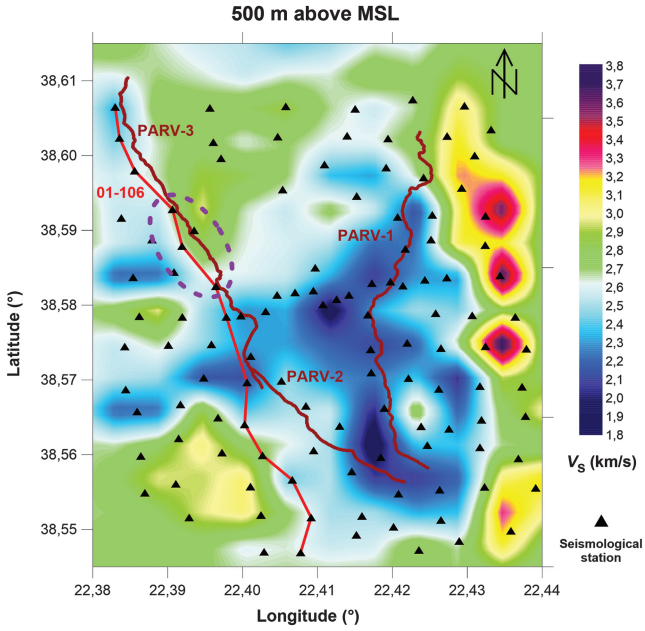

Figure 18. The S-wave velocity (V_S) distribution along the depth slice of 500 m above MSL. The purple ellipse marks the part of the TSI profile 01-106 that is located between the faulting zones noted in Figure 17c. Black triangles represent the Gerolekas-network stations, red line represents the location of the TSI profile 01-106, and brown lines represent the the active-source seismic profiles PARV-1, PARV-2, and PARV-3.

CONCLUSION

We applied a purely earthquake-based passive seismic survey for mineral exploration in a bauxite-producing mining site in Greece. The scope of the survey was the delineation of the expected target depths for the known bauxite-bearing formations. We initially applied LET and managed to obtain a coarse image below a completely unexplored part of the mining site. We reprocessed three lines of legacy active seismic data that existed in the area and showed that the use of the LET velocity model for PreSDM improved the seismic imaging significantly. We then applied TSI by autocorrelation and we retrieved zero-offset virtual reflection responses below each of the recording stations. In this way, we recovered a more detailed image with a vertical resolution of approximately 50 m at the depths of interest, which permitted us to draw conclusions about the location of the target interface. Finally, we jointly interpreted our results and provided an insight on the subsurface below the study area, using a totally environmentally friendly and easy to implement methodology that can be applied even in cases of extreme difficulty in accessibility or environmental sensitivity conditions.

ACKNOWLEDGMENTS

The Gerolekas passive seismic survey was launched in the context of the Smart Exploration action, funded by the European Commission, in the framework of the H2020 "New solutions for sustainable production of raw materials — New sensitive exploration technologies." Smart Exploration has received funding from the European Union's Horizon 2020 research and innovation programme under grant agreement no. 775971. The authors would like to thank Delfi-Distomon S.A. for sharing all available well information and legacy active seismic data of the Gerolekas mining area as well as three anonymous reviewers for their constructive comments that helped improve this manuscript.

DATA AND MATERIALS AVAILABILITY

Data associated with this research are confidential and cannot be released.

APPENDIX A

LET MODEL ROBUSTNESS ASSESSMENT

For the assessment of the Gerolekas LET model robustness, we use two different tools. The first tool is the estimation of a control parameter directly linked to the ray coverage. This parameter is the derivative weighed sum (DWS), which assesses data resolution, or, more precisely, data sufficiency at each unit of the model space (Thurber and Eberhart-Phillips, 1999). The DWS is the number of seismic rays passing through the volume of influence of each model node weighted according to the ray-node separation and the raypath length in the vicinity of the node. This means that the DWS describes the amount of data that actually constrains the velocity value of a specific node during inversion, providing a robust way to distinguish between model areas that are adequately covered by data and areas where insufficient data result in a poorly constrained model.

In Figures A-1 and A-2, we present the obtained DWS distributions for V_P and V_P/V_S, respectively, along depth slices crossing the study area. We visualize depth slices from 500 m above MSL down to 2 km below MSL, where the depth of interest lies. Given the small size of the model cells, we assume for DWS a rather strict value of 100 weighted rays per grid cell, below which we characterize the model space as poorly resolved (white spaces along the depth slices in Figures A-1 and A-2). We can see from Figures A-1 and A-2 that the model space of interest is very well covered by seismic rays — only a very small part located outside the northeast and southwest edges of the inner seismic network on the depth layer of 500 m above MSL is not adequately covered by data. This means that the overall data sufficiency is satisfactory.

However, estimation of the DWS distribution cannot assess the quality of the inversion procedure itself (parameterization, regularization, etc.). For this, we use a second tool — a synthetic reconstruction test using a checkerboard model. Initially introduced by Spakman and Nolet (1988), checkerboard models consist of a regularly alternating pattern of positive and negative anomalies. We construct the checkerboard V_P and V_P/V_S ratio models by applying P-wave velocity perturbations of $\pm 10\%$ on the 1D V_P starting model and V_P/V_S ratio perturbations of $\pm 5\%$ on the uniform V_P/V_S ratio starting model of the field-data inversion (Figure A-3). The percentages of the assumed synthetic velocity perturbations are selected taking into account the range of the calculated V_P and V_P/V_S ratio values from the field-data inversion at the depths of interest. These checkerboard models are used to forward model a synthetic traveltime data set using the same source-receiver geometry and phase distribution as in the case of the field survey. The calculated traveltimes are then subjected to the same inversion procedure as for the field data. The results (Figures A-4 and A-5) are evaluated to assess the procedure's ability to accurately recon-

struct the synthetic checkerboard models. Even though synthetic reconstruction tests suffer from limitations in their ability to assess the quality of an inversion procedure (Lévêque et al., 1993; Rawlinson and Spakman, 2016), they remain the simplest and most widely used tool for qualitatively assessing the reliability of a tomographic model.

Figure A-4 shows that the anomalies of the synthetic model of Figure A-3 in the case of P-wave velocity inversion are reconstructed quite accurately, especially close to the surface, where LET generally suffers from lower resolution. This can be explained by the very dense seismic network, with interstation distances approximately equal to the length of the grid cell used for inversion, resulting in a large number of rays being driven toward the surface as well as the type of the recorded local seismicity — very low-magnitude events occurring at shallow depths. The shallow depths of occurrence create rays that are crossing the shallow model cells at various directions, thus better constraining the estimated model, opposed to the mainly, or even exclusively, subvertical rays expected to be recorded close to the surface from deeper seismicity. Smearing of the anomalies is observed at limited spots, mainly concentrated toward the edges of the examined model space outside the dense inner seismic network or toward the central part of the Gerolekas nappe, which lacked seismic stations. We also observe that the reconstruction of the V_P anomalies in terms of amplitudes seems to be more accurate toward the upper layers in Figure A-4. This might be due to the design of the synthetic reconstruction test because we apply $\pm 10\%$ velocity perturbations on a 1D model that increases with depth. This means that the absolute velocity changes increase at greater depths, which is not necessarily the case in the earth's subsurface. As a result, this observation should be evaluated cautiously and cannot lead to robust conclusions on the inversion's ability to reconstruct the anomalies' amplitudes at depth.

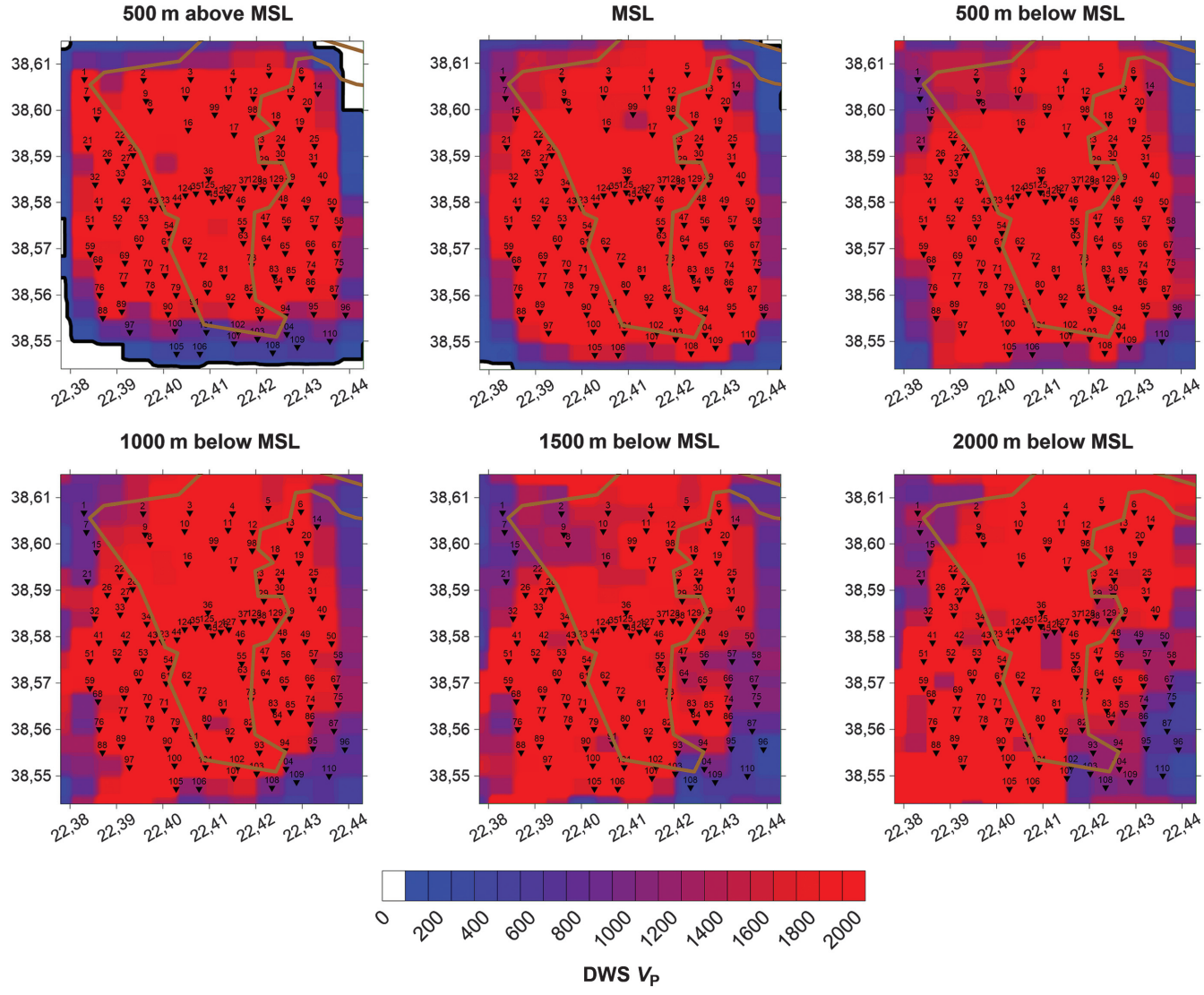

Figure A-1. The DWS distribution of the P-wave velocity inversion along depth slices crossing the study area. The depth slices range from 500 m above MSL to 2 km below MSL. Black triangles represent the Gerolekas-network station, and brown line represents the superficial appearance of the Gerolekas nappe.

Downloaded 12/28/23 to 77.169.250.78. Redistribution subject to SEG license or copyright; see Terms of Use at http://library.seg.org/page/policies/terms
DOI:10.1190/geo2023-0213.1

Downloaded 12/28/23 to 77.169.250.78. Redistribution subject to SEG license or copyright; see Terms of Use at http://library.seg.org/page/policies/terms
DOI:10.1190/geo2023-0213.1

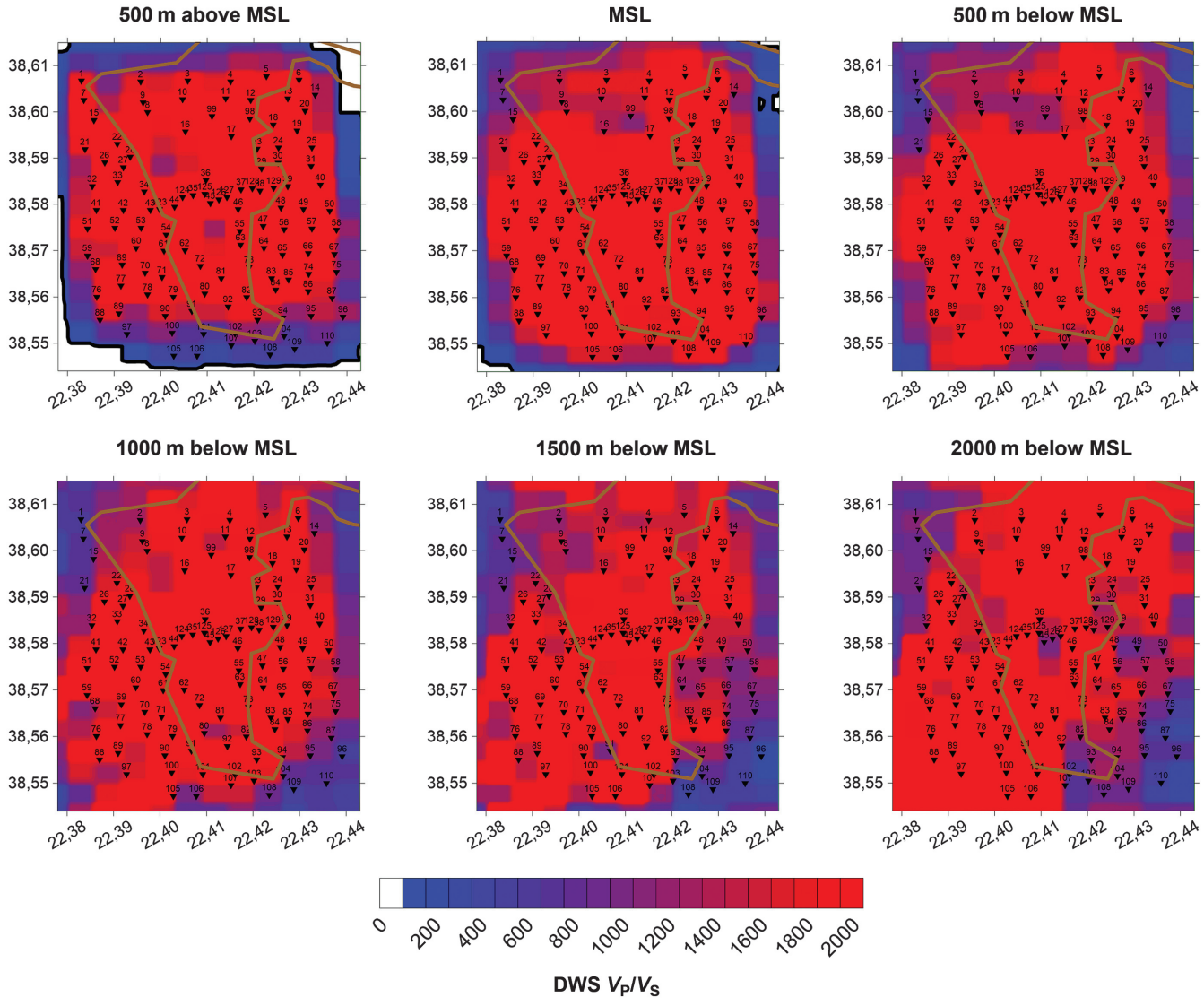

Figure A-2. As shown in Figure A-1 but for the V_P/V_S ratio.

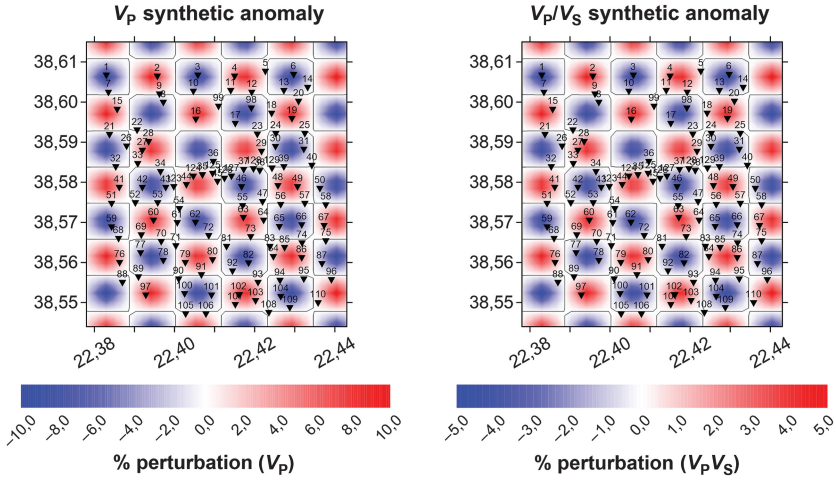

Figure A-3. Checkerboard models used for synthetic reconstruction testing of the Gerolekas tomographic inversion. The models consist of alternating perturbations of ±10% of the V_P value of the reference 1D starting model and ±5% of the reference V_P/V_S ratio value. Black triangles represent the Gerolekas-network stations.

Downloaded 12/28/23 to 77.169.250.78. Redistribution subject to SEG license or copyright; see Terms of Use at http://library.seg.org/page/policies/terms
DOI:10.1190/geo2023-0213.1

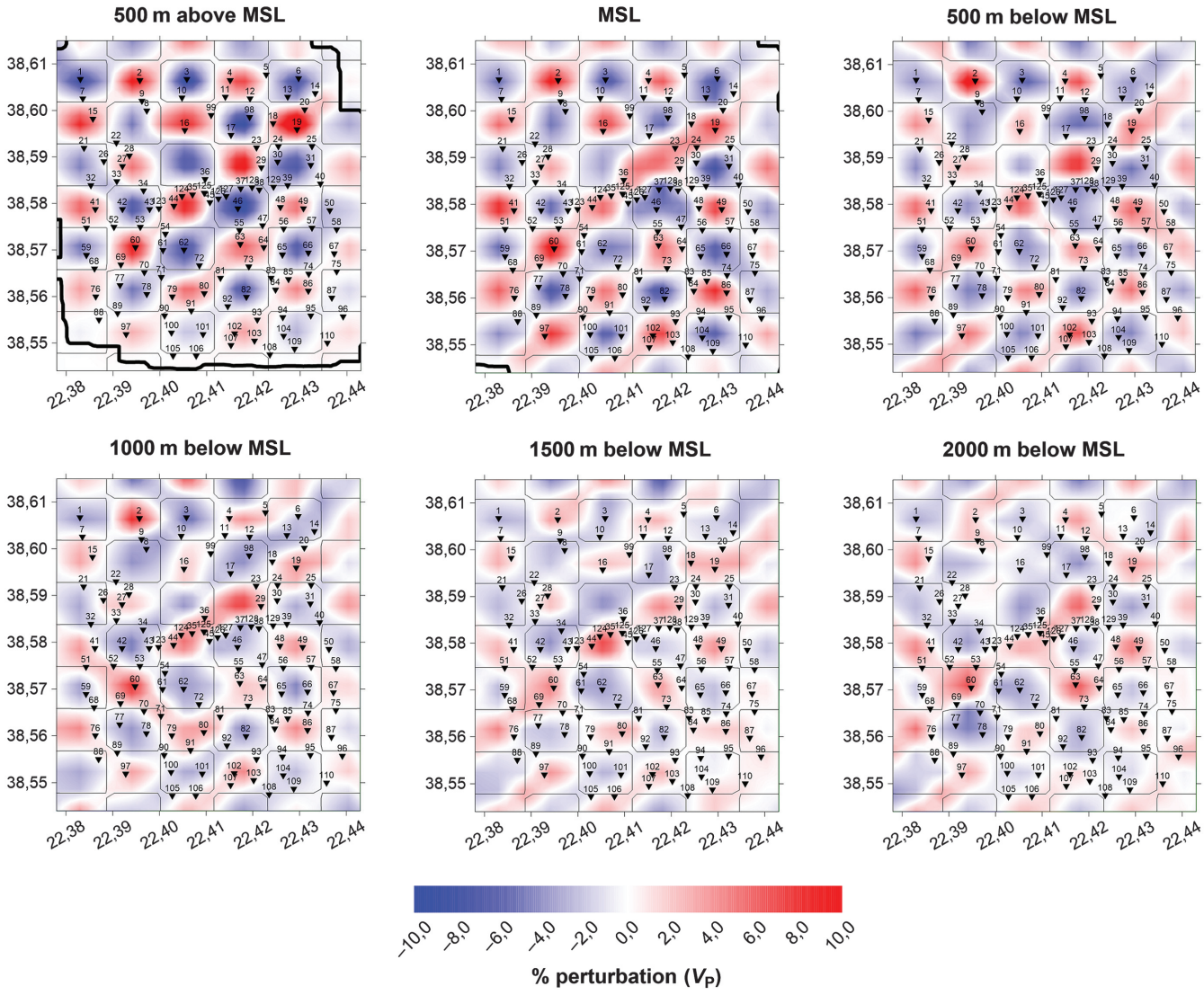

Figure A-4. Inverted P-wave velocity models of the checkerboard test along depth slices crossing the study area. The depth slices range from 500 m above MSL to 2 km below MSL. Black triangles represent the Gerolekas-network stations, and thick black line represents the iso-DWS contour equal to 100 (see Figure A-1).

In the case of Figure A-5, we observe that the V_P/V_S ratio model reconstruction is acceptable but clearly less accurate than the reconstruction of the respective P-wave velocity model, in terms of delineation of the geometry and estimation of the amplitudes of the anomalies. The calculated V_P/V_S ratio values are generally underestimated throughout the inverted volume, and this underestimation has no dependence on the depth, as in the case of P-wave velocity, indicating that the amplitudes of the estimated V_P/V_S ratio values of the field data also might be underestimated. Moreover, even though the general form of the alternating high-low anomalies is reconstructed, we observe some smearing not only at the places that are not covered by seismic stations but also along the diagonal of the synthetic model, where no anomaly alternation occurs between neighboring grid cells, and more precisely toward a northeast–southwest direction. This relatively lower performance of the V_P/V_S ratio inversion can be attributed to two reasons: (1) the higher uncertainty in the S-wave onset time picking, which results in down-weighted S-wave arrivals during the inversion procedure and (2) the relatively lower number of S-wave first arrivals in the data set, especially in the case of the low-magnitude events occurring at shallow depths, which are the major contributors to the reconstruction of the shallower parts of the V_P/V_S ratio model.

APPENDIX B

PROCESSING WORKFLOW FOR TSI BY AUTOCORRELATION

Following the procedure proposed in Polychronopoulou et al. (2020):

1) For each station of the recording seismic network, we isolate the selected events and extract the useful signal from the continuous records. We use the previously estimated P- and

Downloaded 12/28/23 to 77.169.250.78. Redistribution subject to SEG license or copyright; see Terms of Use at http://library.seg.org/page/policies/terms
DOI:10.1190/geo2023-0213.1

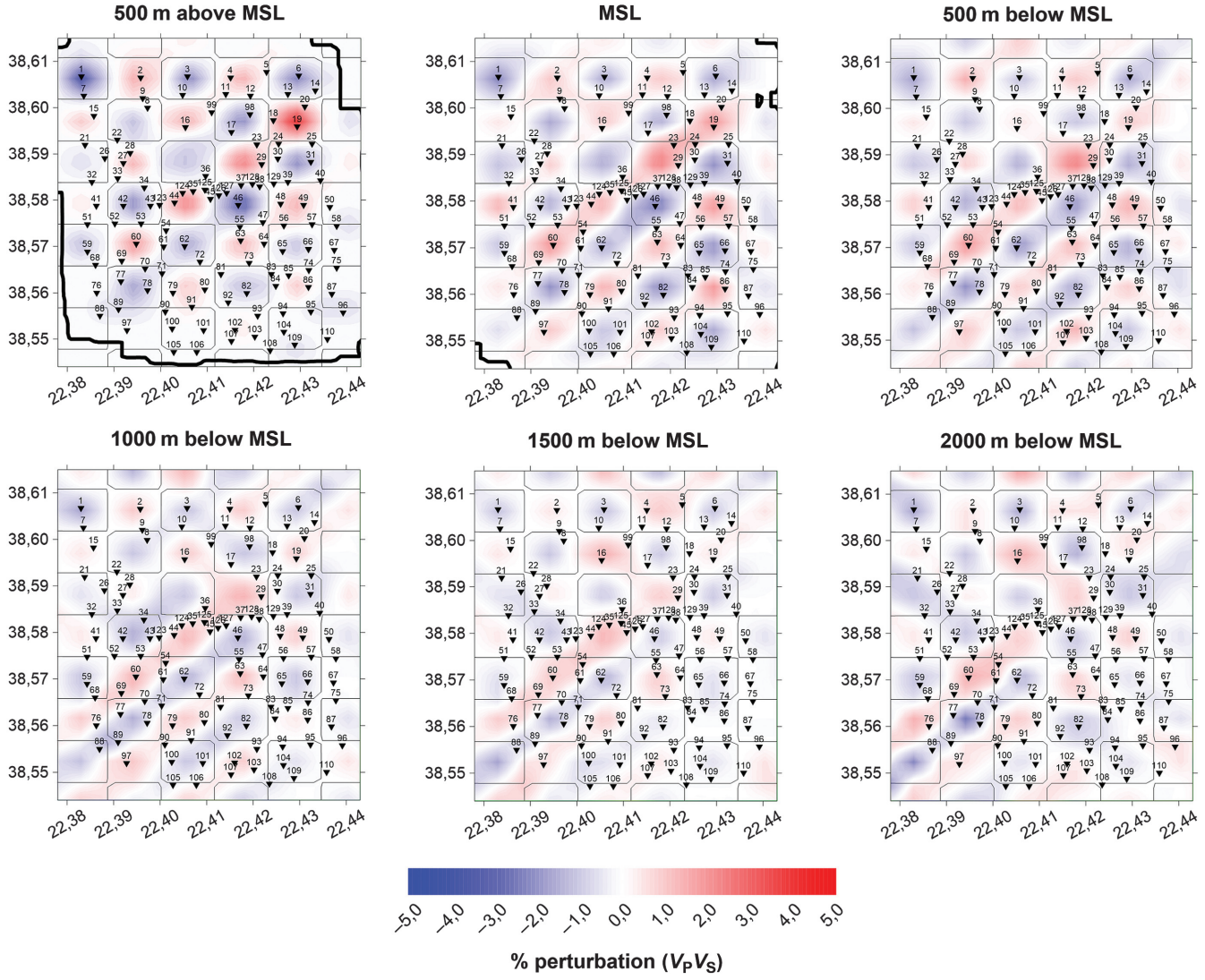

Figure A-5. As shown in Figure A-4 but for the V_P/V_S ratio.

S-wave first-arrival times to define adequate windows for the extraction of the P- and the S-wave coda. The P-wave coda is accurately extracted from the vertical component, using a window equal to the time interval between the P- and S-wave first arrivals of each of the selected microearthquakes, whereas the S-wave coda, which is characterized by more ambiguity, is extracted from the horizontal components, assuming it starts at the moment of the S-wave first-arrival time and using a window length equal to the extracted P-wave coda from the same microearthquake.

2) For each component separately, we amplitude normalize the extracted signals and calculate their autocorrelation functions (ACFs). These autocorrelograms for all selected microearthquakes for a station are then stacked per component and the result of the summation is used to define a spiking deconvolution operator, using the Levinson-Durbin recursion algorithm (Ljung, 1987).
3) We apply spiking deconvolution on the original signals to enhance their vertical resolution by flattening the spectrum in the interval of interest.
4) We calculate the autocorrelation of the deconvolved signals.
5) We stack the estimated autocorrelograms of the deconvolved signals per component for each station over the microearthquakes selected for that station.

REFERENCES

Abu Zeid, N., E. Corradini, S. Bignardi, V. Nizzo, and G. Santarato, 2017, The passive seismic technique 'HVSR' as a reconnaissance tool for mapping paleo-soils: The case of the Pilastri Archaeological Site, Northern Italy: Archaeological Prospection, **24**, 245–258, doi: 10.1002/arp.1568.

Capizzi, P., and R. Martorana, 2022, Analysis of HVSR data using a modified centroid-based algorithm for near-surface geological reconstruction: Geosciences, **12**, 147, doi: 10.3390/geosciences12040147.

Casas, J. A., G. A. Badi, L. Franco, and D. Draganov, 2020, Seismic interferometry applied to regional and teleseismic events recorded at Planchón-Peteroa Volcanic Complex, Argentina-Chile: Journal of Volcanology and Geothermal Research, **393**, 106805, doi: 10.1016/j.jvolgeores.2020.106805.

Chamarczuk, M., M. Malinowski, and D. Draganov, 2021, 2D body-wave seismic interferometry as a tool for reconnaissance studies and optimization of passive reflection seismic surveys in hardrock environments: Journal of Applied Geophysics, **187**, 104288, doi: 10.1016/j.jappgeo.2021.104288.

Downloaded 12/28/23 to 77.169.250.78. Redistribution subject to SEG license or copyright; see Terms of Use at http://library.seg.org/page/policies/terms
DOI:10.1190/geo2023-0213.1

Cheraghi, S., A. J. Craven, and G. Bellefleur, 2015, Feasibility of virtual source reflection seismology using interferometry for mineral exploration: A test study in the Lalor Lake VMS mining area, Manitoba, Canada: Geophysical Prospecting, **63**, 833–848, doi: 10.1111/1365-2478.12244.

Claerbout, J. F., 1968, Synthesis of a layered medium from its acoustic transmission response: Geophysics, **33**, 264–269, doi: 10.1190/1.1439927.

Cohen, J. K., and J. W. Stockwell Jr., 2008, CWP/SU: Seismic Un*x Release No. 44R14: An open-source software package for seismic research and processing: Center for Wave Phenomena: Colorado School of Mines.

Daneshvar, M. R., C. S. Clay, and M. K. Savage, 1995, Passive seismic imaging using microearthquakes: Geophysics, **60**, 1178–1186, doi: 10.1190/1.1443846.

Donoso, G. A., A. Malehmir, N. Pacheco, V. Araujo, M. Penney, J. Carvalho, B. Spicer, and S. Beach, 2020, Potential of legacy 2D seismic data for deep targeting and structural imaging at the Neves-Corvo massive sulphide-bearing deposit, Portugal: Geophysical Prospecting, **68**, 44–61, doi: 10.1111/1365-2478.12861.

Draganov, D., X. Campman, J. Thorbecke, A. Verdel, and K. Wapenaar, 2009, Reflection images from ambient seismic noise: Geophysics, **74**, no. 5, A63–A67, doi: 10.1190/1.3193529.

Eberhart-Phillips, D., 1986, Three-dimensional velocity structure in northern California Coast Ranges from inversion of local earthquake arrival times: Bulletin of the Seismological Society of America, **76**, 1025–1052, doi: 10.1785/BSSA0760041025.

Eberhart-Phillips, D., 1990, Three-dimensional P and S velocity structure in the Coalinga region, California: Journal of Geophysical Research: Solid Earth, **95**, 15343–15363, doi: 10.1029/JB095iB10p15343.

Evans, J. R., D. Eberhart-Phillips, and C. H. Thurber, 1994, User's manual for SIMULPS12 for imaging Vp and Vp/Vs: A derivative of the "Thurber" tomographic inversion SIMUL3 for local earthquakes and explosions: Open File Report 94-431, U.S. Geological Survey.

Giannopoulos, D., A. Lois, K. Leontarakis, K. Polychronopoulou, N. Martakis, S. Calassou, M. Collin, S. Chevrot, M. Sylvander, A. Villaseñor, J. Diaz, and A. Bitri, 2019, The MAUPASACQ experiment: Preliminary results of a noise-based Rayleigh wave analysis of the Mauleon Basin in western Pyrenees, France: Geophysical Research Abstracts, 21, EGU2019-12707.

Latorre, D., J. Virieux, T. Monfret, V. Monteiller, T. Vanorio, J.-L. Got, and H. Lyon-Caen, 2004, A new seismic tomography of Aigion area (Gulf of Corinth, Greece) from the 1991 data set: Geophysical Journal International, **159**, 1013–1031, doi: 10.1111/j.1365-246X.2004.02412.x.

Lee, W. H. K., and S. W. Stewart, 1981, Principals and applications of microearthquake networks: Academic Press Inc.

Leontarakis, K., A. Lois, A. Pantazopoulos, and K. Polychronopoulou, 2015, A comprehensive methodology for automated analysis of seismic records and its contribution to a passive seismic tomography survey in Delvina, SW Albania: 85th Annual International Meeting, SEG, Expanded Abstracts, 2563–2567, doi: 10.1190/segam2015-5897135.1.

Lévêque, J. J., L. Rivera, and G. Wittlinger, 1993, On the use of the checkerboard test to assess the resolution of tomographic inversions: Geophysical Journal International, **115**, 313–318, doi: 10.1111/j.1365-246X.1993.tb05605.x.

Ljung, L., 1987, System identification: Theory for the user: Prentice-Hall, 278–280.

Lois, A., E. Sokos, N. Martakis, P. Paraskevopoulos, and G.-A. Tselentis, 2013, A new automatic S-onset detection technique: Application in local earthquake data: Geophysics, **78**, no. 1, KS1–KS11, doi: 10.1190/geo2012-0050.1.

Malehmir, A., G. Donoso, M. Markovic, G. Maries, L. Dynesius, B. Brodic, N. Pecheco, P. Marsden, E. Bäckström, M. Penney, and V. Araujo, 2019, Smart exploration: From legacy data to state-of-the-art data acquisition and imaging: First Break, **37**, 71–74, doi: 10.3997/1365-2397.n0049.

Manzi, M., A. Malehmir, and R. Durrheim, 2019, Giving the legacy seismic data the attention they deserve: First Break, **37**, 89–96, doi: 10.3997/1365-2397.n0050.

Morgan, D., D. Gunn, A. Payo, and M. Raines, 2022, Passive seismic surveys for beach thickness evaluation at different England (UK) sites: Journal of Marine Science and Engineering, **10**, 667, doi: 10.3390/jmse10050667.

Morton, S. L., J. Ivanov, S. L. Peterie, R. D. Miller, and A. J. Livers-Douglas, 2021, Passive multichannel analysis of surface waves using 1D and 2D receiver arrays: Geophysics, **86**, no. 6, EN63–EN75, doi: 10.1190/geo2020-0104.1.

Nakata, N., R. Snieder, and M. Behm, 2014, Body-wave interferometry using regional earthquakes with multidimensional deconvolution after wavefield decomposition at free surface: Geophysical Journal International, **199**, 1125–1137, doi: 10.1093/gji/ggu316.

Nishitsuji, Y., S. Minato, B. Boullenger, M. Gòmez, K. Wapenaar, and D. Draganov, 2016b, Crustal-scale reflection imaging and interpretation by passive seismic interferometry using local earthquakes: Interpretation, **4**, no. 3, SJ29–SJ53, doi: 10.1190/INT-2015-0226.1.

Nishitsuji, Y., E. Ruigrok, M. Gomez, K. Wapenaar, and D. Draganov, 2016a, Reflection imaging of aseismic zones of the Nazca slab by global-phase seismic interferometry: Interpretation, **4**, no. 3, SJ1–SJ16, doi: 10.1190/INT-2015-0225.1.

Orfanos, C., K. Leontarakis, A. Lois, K. Polychronopoulou, and N. Martakis, 2016, Automatic passive seismic data processing with no prior information: The contribution of surface wave tomography: First Break, **34**, 75–84, doi: 10.3997/1365-2397.34.7.86053.

Orfanos, C., K. Leontarakis, K. Polychronopoulou, G. Apostolopoulos, K. Athanasas, and N. Martakis, 2021, An integrated feasibility study using passive geophysical methods for the investigation of the Gerolekas bauxite deposits site, Greece: Near Surface Geophysics, **20**, 607–622, doi: 10.1002/nsg.12181.

Panea, I., D. Draganov, C. Almagro Vidal, and V. Mocanu, 2014, Retrieval of reflections from ambient noise recorded in the Mizil area, Romania: Geophysics, **79**, no. 3, Q31–Q42, doi: 10.1190/geo2013-0292.1.

Polychronopoulou, K., A. Lois, and D. Draganov, 2020, Body-wave passive seismic interferometry revisited: Mining exploration using the body waves of local microearthquakes: Geophysical Prospecting, **68**, 232–253, doi: 10.1111/1365-2478.12884.

Polychronopoulou, K., A. Lois, N. Martakis, S. Calassou, and D. Draganov, 2019a, Earthquake-based passive seismic exploration techniques: 89th Annual International Meeting, SEG, Expanded Abstracts, 5393–5397, doi: 10.1190/segam2019-w21-04.1.

Polychronopoulou, K., and N. Martakis, 2016, Getting the most out of passive seismic tomography: The case of the Delvina gas field exploration project: 6th EAGE Workshop on Passive Seismic, doi: 10.3997/2214-4609.201600022.

Polychronopoulou, K., C. Orfanos, N. Martakis, and D. Draganov, 2019b, Preliminary results of an integrated passive seismic survey at the Gerolekas bauxite mining site — Central Greece: 25th European Meeting of Environmental and Engineering Geophysics, EAGE, Extended Abstracts, doi: 10.3997/2214-4609.201902374.

Rawlinson, N., and W. Spakman, 2016, On the use of sensitivity tests in seismic tomography: Geophysical Journal International, **205**, 1221–1243, doi: 10.1093/gji/ggw084.

Romero, P., and M. Schimmel, 2018, Mapping the basement of the Ebro Basin in Spain with seismic ambient noise autocorrelations: Journal of Geophysical Research: Solid Earth, **123**, 5052–5067, doi: 10.1029/2018JB015498.

Sachpazi, M., A. Galvé, M. Laigle, A. Hirn, E. Sokos, A. Serpetsidaki, J.-M. Marthelot, J. M. Pi Alperin, B. Zelt, and B. Taylor, 2007, Moho topography under central Greece and its compensation by Pn time-terms for the accurate location of hypocenters: The example of the Gulf of Corinth 1995 Aigion earthquake: Tectonophysics, **440**, 53–65, doi: 10.1016/j.tecto.2007.01.009.

Saragiotis, C. D., L. J. Hadjileontiadis, and S. M. Panas, 2002, PAI-S/K: A robust automatic seismic P phase arrival identification scheme: IEEE Transactions on Geoscience and Remote Sensing, **40**, 1395–1404, doi: 10.1109/TGRS.2002.800438.

Spakman, W., and G. Nolet, 1988, Imaging algorithms, accuracy and resolution in delay time tomography, *in* N. J. Vlaar, G. Nolet, M. J. R. Wortel, and S. A. P. Cloetingh, eds., Mathematical geophysics: A survey of recent developments in seismology and geodynamics: Springer, 155–187.

Thurber, C., and D. Eberhart-Phillips, 1999, Local earthquake tomography with flexible gridding: Computers & Geosciences, **25**, 809–818, doi: 10.1016/S0098-3004(99)00007-2.

Thurber, C. H., 1983, Earthquake locations and three-dimensional crustal structure in Coyote Lake area, Central California: Journal of Geophysical Research: Solid Earth, **88**, 8226–8236, doi: 10.1029/JB088iB10p08226.

Um, J., and C. H. Thurber, 1987, A fast algorithm for two-point seismic ray tracing: Bulletin of the Seismological Society of America, **77**, 972–986, doi: 10.1785/BSSA0770030972.

Wapenaar, K., D. Draganov, R. Snieder, X. Campman, and A. Verdel, 2010, Tutorial on seismic interferometry: Part 1 — Basic principles and applications: Geophysics, **75**, no. 5, A195–A209, doi: 10.1190/1.3457445.

Zhang, J., and M. Nafi Toksöz, 1998, Nonlinear refraction traveltime tomography: Geophysics, **63**, 1726–1737, doi: 10.1190/1.1444468.

Biographies and photographs of the authors are not available.